JEM Journal of Experimental Medicine

ARTICLE

Leukemogenic Kras mutation reprograms multipotent progenitors to facilitate its spread through the hematopoietic system

Geunhyo Jang[1], Rosa Park[2], Eduardo Esteva[1,3], Pei-Feng Hsu[1], Jue Feng[1], Samik Upadhaya[1], Catherine M. Sawai[4], Iannis Aifantis[1], David R. Fooksman[2], and Boris Reizis[1]

Leukemia-driving mutations are thought to arise in hematopoietic stem cells (HSC), yet the natural history of their spread is poorly understood. We genetically induced mutations within endogenous murine HSC and traced them in unmanipulated animals. In contrast to mutations associated with clonal hematopoiesis (such as *Tet2* deletion), the leukemogenic *Kras*^{G12D} mutation dramatically accelerated HSC contribution to all hematopoietic lineages. The acceleration was mediated by *Kras*^{G12D}-expressing multipotent progenitors (MPP) that lacked self-renewal but showed increased proliferation and aberrant transcriptome. The deletion of osteopontin, a secreted negative regulator of stem/progenitor cells, delayed the early expansion of mutant progenitors. *Kras*^{G12D}-carrying cells showed increased CXCR4-driven motility in the bone marrow, and the blockade of CXCR4 reduced the expansion of MPP in vivo. Finally, therapeutic blockade of KRAS^{G12D} spared mutant HSC but reduced the expansion of mutant MPP and their mature progeny. Thus, transforming mutations facilitate their own spread from stem cells by reprogramming MPP, creating a preleukemic state via a two-component stem/progenitor circuit.

Introduction

The blood comprises diverse cell lineages including platelets, erythrocytes, short-lived myeloid cells including monocytes and granulocytes, and long-lived lymphocytes. This entire spectrum is continuously generated in the bone marrow (BM) of mammals from adult hematopoietic stem cells (HSC), the unique multipotent cell type capable of self-renewal (Eaves, 2015). The rare "top-level" HSC give rise to short-term HSC (ST-HSC) and multipotent progenitors (MPP), the non-renewing multipotent cell types that progressively differentiate into lineage- and cell type–committed progenitors and mature cells (Laurenti and Göttgens, 2018). Although originally based on transplantation studies, this HSC-driven hierarchical model of hematopoiesis has been recently confirmed to reflect native hematopoiesis in unmanipulated animals (Pucella et al., 2020) and humans (Sankaran et al., 2022). In particular, genetic labeling and tracing of endogenous murine HSC revealed their continuous multilineage contribution to hematopoiesis in the steady state (Busch et al., 2015; Chapple et al., 2018; Sawai et al., 2016; Säwen et al., 2018). Importantly, this process can be dynamically modulated by environmental stimuli and pathological conditions (Collins et al., 2021): for example, the multilineage contribution of HSC is accelerated by interferon response (Sawai et al., 2016), whereas bacterial infections spare HSC but accelerate the differentiation of MPP (Fanti et al., 2023).

The well-balanced hierarchy of hematopoiesis can be disrupted by genetic lesions that arise in HSC and/or their progeny. Thus, age-related clonal hematopoiesis (ARCH) involves the expansion of specific cell clones within the hematopoietic system. ARCH is common in elderly humans who are otherwise healthy, although it is thought to increase the risk of leukemia and cardiovascular disease (Ahmad et al., 2023; Warren and Link, 2020; Weeks and Ebert, 2023). Cell clones expanded in ARCH often carry inactivating mutations in epigenetic regulators such as methylcytosine dioxygenase TET2 or DNA methyltransferase DNMT3A. These mutations are thought to arise in HSC and increase their competitive fitness (Yamashita et al., 2020), especially in the inflammatory environment (Avagyan and Zon, 2023; King et al., 2020). In contrast, another set of

[1]Department of Pathology, New York University Grossman School of Medicine, New York, NY, USA; [2]Department of Pathology, Albert Einstein College of Medicine, Bronx, NY, USA; [3]Applied Bioinformatics Laboratories, New York University Grossman School of Medicine, New York, NY, USA; [4]INSERM Unit 1312 BRIC, University of Bordeaux, Bordeaux, France.

Correspondence to Boris Reizis: boris.reizis@nyulangone.org

J. Feng's current affiliation is Department of Pharmacological Sciences, Icahn School of Medicine at Mount Sinai, New York, NY, USA. S. Upadhaya's current affiliation is Cancer Research Institute, New York, NY, USA.

mutations is found almost exclusively in neoplastic conditions including myelodysplastic syndrome, leukemia, and lymphoma (Kishtagari et al., 2020). These mutations often block differentiation (e.g., those in key hematopoietic transcription factors such as RUNX1) or enhance signaling cascades leading to cell proliferation, such as activating mutation of the FLT3 receptor or of RAS proteins (KRAS or NRAS). Indeed, stepwise accumulation of these two classes of mutations in HSC is thought to cause eventual emergence of fully transformed leukemic clones (Miles et al., 2020; Morita et al., 2020; Schwede et al., 2023, *Preprint*).

The distinct pathogenic consequences of ARCH-associated (e.g., Tet2 loss) and leukemia-associated (e.g., RAS activation) mutations can be recapitulated in mouse models. For example, the deletion of *Tet2* causes myeloproliferative disease with a long latency (Li et al., 2011; Moran-Crusio et al., 2011; Quivoron et al., 2011), which can be accelerated by microbial stimulation (Meisel et al., 2018). In contrast, the activation of RAS signaling in hematopoietic cells, e.g., by inducing the activating $KRAS^{G12D}$ mutation, causes a variety of leukemia types (Braun et al., 2004; Chan et al., 2004; Dail et al., 2010; Sabnis et al., 2009; Tarnawsky et al., 2017). In these models, mutations are simultaneously present in the entire hematopoietic system, circumventing the natural process as it occurs in human patients. To understand the early effects of ARCH- and leukemia-associated mutations on normal hematopoiesis, it is imperative to model their stepwise initiation and progression. To this end, the mutations need to be introduced specifically into endogenous HSC, and their spread throughout the hematopoietic system should be characterized by lineage tracing.

Here, we used Cre recombination to induce prototypical leukemia-associated ($KRAS^{G12D}$) or ARCH-associated (TET2 loss) mutations specifically in HSC and trace the mutant HSC population in their native hosts. In contrast to minimal effects of ARCH mutations, $Kras^{G12D}$ dramatically accelerated HSC contribution in the steady state, with the mutation rapidly spreading throughout the hematopoietic system prior to leukemia development. Unexpectedly, this accelerated contribution commenced at the MPP stage and was facilitated by a profound reprogramming of progenitor physiology, including their increased CXCR4-driven motility. The results emphasize the ability of leukemia-associated mutations to reprogram the normal hematopoietic differentiation, converting HSC into their "reservoirs" and progenitors into "super-spreaders."

Results

$Kras^{G12D}$ mutation in HSC accelerates their contribution to hematopoiesis

We have previously generated *Pdzklip1*-CreER transgenic mice expressing tamoxifen-inducible Cre recombinase (CreER) specifically in HSC. When crossed with a reporter allele expressing red fluorescent protein tdTomato (Tom) in a Cre-inducible manner ($R26^{Tom}$), the resulting reporter mice allow specific labeling of HSC with Tom and tracing their contribution to progenitors and mature cells (Sawai et al., 2016). We crossed *Pdzklip1*-CreER $R26^{Tom/Tom}$ reporter mice with $Kras^{G12D}$ Lox-Stop-Lox (LSL) strain (Jackson et al., 2001), in which Cre recombination activates the expression of the constitutively active $KRAS^{G12D}$ protein. Importantly, $KRAS^{G12D}$ is expressed from the endogenous *Kras* allele and thus is under its normal transcriptional regulation (Tuveson et al., 2004) (Fig. 1 A). In the resulting *Pdzklip1*-CreER $R26^{Tom/Tom}$ $Kras^{G12D}$ reporter mice, tamoxifen-induced Cre recombination is predicted to activate both $Kras^{G12D}$ and Tom in HSC, allowing the tracing of mutation-carrying HSC (Fig. 1 A). To confirm that, *Pdzklip1*-CreER $R26^{Tom/Tom}$ $Kras^{G12D}$ mice were administered a single dose of tamoxifen, and 3 wk later used to sort lineage marker–negative (Lin^-) $Sca\text{-}1^+$ $c\text{-}Kit^+$ (LSK) population, which contains HSC ($CD150^+$ $CD48^-$), ST-HSC ($CD150^-$ $CD48^-$), and MPP ($CD150^-$ $CD48^+$). Tom^+ but not Tom^- LSK cells showed extensive recombination of the $Kras^{G12D}$ allele, validating Tom expression as a marker of mutation-carrying cells at this time point (Fig. 1 B). The recombined $Kras^{G12D}$ allele became detectable in total BM Tom^- cells at 5 wk (in one out of four mice) and 7 wk (in all mice) (Fig. S1 A), likely reflecting a strong selection for rare Tom^- Kras-mutant cells over time. However, $Kras^{G12D}$ recombination was much more extensive in Tom^+ versus Tom^- cells at these time points (Fig. S1 B), supporting the correlation between *Kras* mutation and Tom expression within the first several weeks after induction. As expected, tamoxifen-treated *Pdzklip1*-CreER $R26^{Tom/Tom}$ $Kras^{G12D}$ mice became moribund with a median survival of 18 wk (Fig. 1 C), showing features of acute T-lymphoblastic leukemia (T-ALL) including splenomegaly and massively enlarged thymus (Fig. S1 C). We then tested the effect of $Kras^{G12D}$ induction in HSC on hematopoiesis within 4–12 wk after induction (Fig. 1 D). We found that the accrual of Tom^+ cells was dramatically accelerated in the peripheral blood (PB) of $Kras^{G12D}$ compared with wild-type (WT) reporter mice, with significant increases in most lineages by 4 wk after induction, and in all lineages including T cells by 8 wk (Fig. 1 E).

To better characterize the accelerated differentiation of Kras-mutant HSC, we analyzed mice at 2- to 7-wk endpoints. At 2 wk after induction, mature immune cells in the spleen (Fig. 1 F) and BM (Fig. 1 G) showed the expected absence of labeling in both $Kras^{G12D}$ and WT reporter mice. However, the labeling of all cell types in $Kras^{G12D}$ mice became significantly increased at 3 wk and reached high levels by 5 wk, showing an ∼20-fold increase in myeloid cells, ∼60–80-fold increase in natural killer (NK) cells, and ∼120–160-fold increase in B cells compared with WT (Fig. 1, F and G). The resulting labeling efficiencies of 60–70% at 7 wk (Fig. S1, D and E) are typically attained in WT mice by 8–9 mo after labeling (Sawai et al., 2016). As described previously (Sawai et al., 2016), WT reporters showed minimal labeling of the early thymic progenitors (ETP) or the downstream thymocyte subsets at 3–5 wk (Fig. 1 H) and up to 7 wk (Fig. S1 F). In contrast, all $Kras^{G12D}$ reporter mice showed detectable (∼5%) ETP labeling at 3 wk and massive (>50%) labeling at 5 wk, along with comparably high labeling in $CD4^-CD8^-$ double-negative (DN2/3 and DN4) and $CD4^+CD8^+$ double-positive (DP) thymocytes. At 7 wk, the labeling of DP thymocytes reached or exceeded that of HSC and also spread into mature single-positive $CD4^+$ and $CD8^+$ thymocytes (Fig. S1, F and G). This massive expansion likely is a consequence of enhanced HSC contribution to

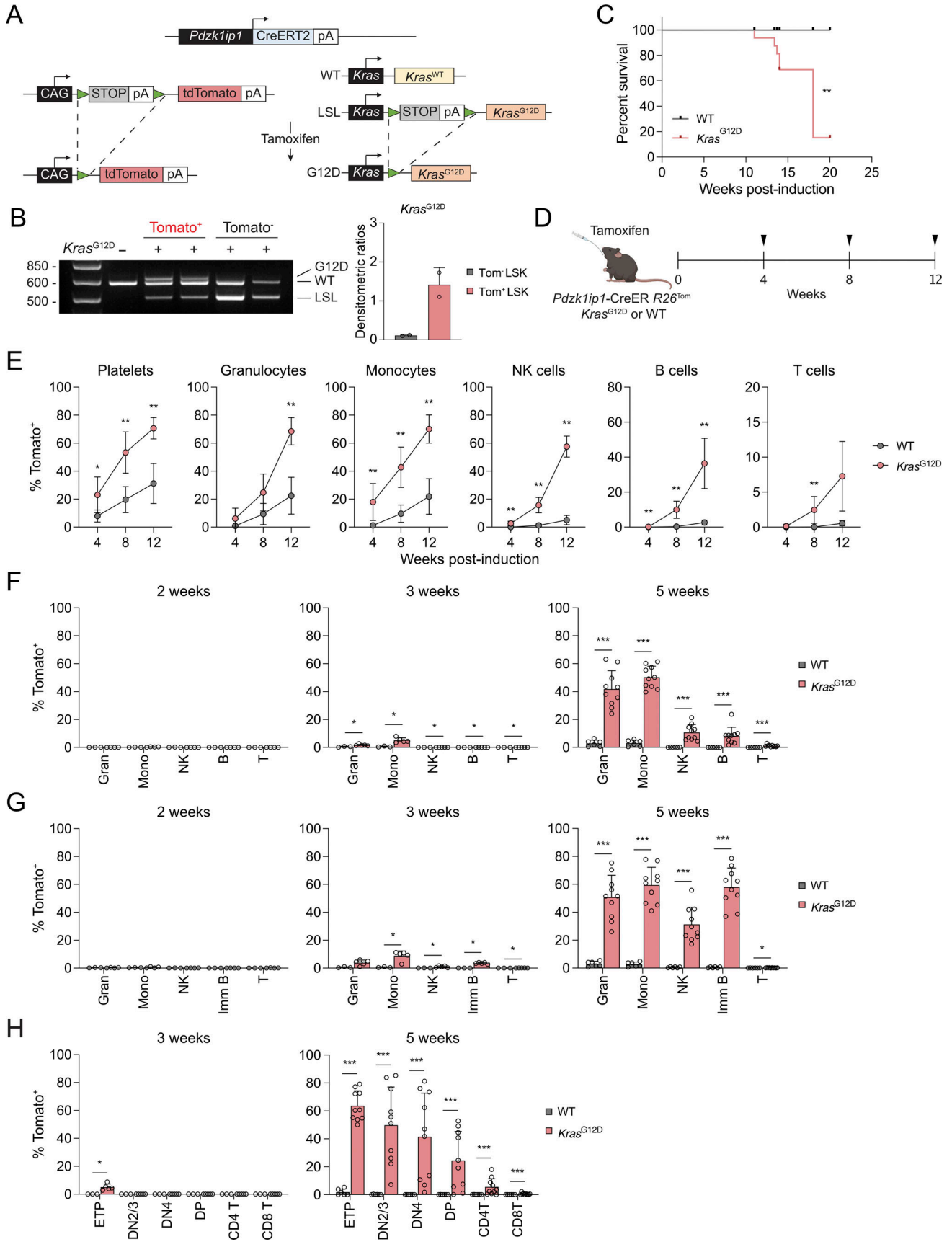

Figure 1. ***Kras*^{G12D}-mutant HSC show accelerated multilineage contribution.** HSC-specific Cre reporter mice (*Pdzk1ip1*-CreER *R26*$^{Tom/Tom}$) that carried WT or conditional mutant (*Kras*^{G12D}) *Kras* alleles were administered a single dose of tamoxifen to induce simultaneous Tom expression and *Kras* mutation in HSC.

(A) Schematic of the alleles and their recombination following tamoxifen administration. The transcriptional stop cassettes containing polyadenylation signals (STOP/pA) and the LoxP sites (green triangles) are shown. For the endogenous *Kras* alleles, the WT, the conditional unrecombined LSL, and the recombined mutant (G12D) alleles are shown. **(B)** Recombination of conditional *Kras* allele in Tom$^+$ or Tom$^-$ LSK cells sorted from the BM 3 wk after tamoxifen treatment. The left panel shows genomic PCR results for two independent animals, with the amplicons for *Kras* alleles (A) and sizes of DNA size markers (in base pairs) indicated. The right panel shows densitometric ratios of the recombined (G12D) to unrecombined (LSL) amplicons. Symbols represent individual mice; bars represent the mean ± range. **(C)** Kaplan–Meier plot of animal survival over the indicated time after tamoxifen administration (n = 16 for *Kras*^{G12D} and 12 for WT mice). **(D)** Lineage tracing of *Kras*^{G12D}-mutant HSC. Reporter mice were monitored for Tom expression in PB every 4 wk for up to 12 wk. **(E)** Accrual of Tom$^+$ cells in the blood. Shown are fractions of Tom$^+$ cells within the indicated blood cell types in *Pdzk1ip1*-CreER *R26*$^{Tom/Tom}$ *Kras*^{G12D} or WT reporter mice after tamoxifen treatment. Symbols represent the mean ± SD of five to six mice per group. **(F–H)** Analysis of reporter mice at the indicated endpoint. Shown are the fractions of Tom$^+$ cells within immune cell types in the spleen (F) and the BM (G), and within subsets of thymocytes (H). Symbols represent individual mice; bars represent the mean ± SD of data from a single experiment (weeks 2–3) or from two experiments (week 5). Statistical significance was estimated by the Mantel–Cox test (C) or the Mann–Whitney test (other panels). *P < 0.05, **P < 0.01, ***P < 0.001. Source data are available for this figure: SourceData F1.

thymopoiesis, although the expansion of a very rare labeled thymic progenitor cannot be ruled out. The activation of Kras was shown to circumvent the β-selection checkpoint, which ensures that only those thymocytes that productively rearranged their TCRβ chain progress from CD25$^+$ DN3 to CD25$^-$ DN4 and DP stages (Kortum et al., 2013). Accordingly, the DN3 population in the thymi of induced *Kras*^{G12D} reporter mice was reduced in favor of a CD25^{int} population (Fig. S1 H); moreover, the acquisition of intracellular TCRβ at the DN4 and subsequent stages was abolished in these mice (Fig. S1, I and J). These data suggest a failure of β-selection in *Kras*^{G12D}-expressing thymocytes, likely contributing to the subsequent development of T-ALL. Overall, the acquisition of activating Kras mutation by HSC causes a dramatic acceleration of their contribution to all hematopoietic lineages, leading to the rapid spread of the mutation prior to leukemogenesis.

To test whether similar acceleration is caused by mutations associated with ARCH, we generated *Pdzk1ip1*-CreER *R26*$^{Tom/Tom}$ reporter animals that also carried LoxP-flanked (floxed) conditional null allele of *Tet2* (*Tet2*$^{fl/fl}$) (Moran-Crusio et al., 2011). No difference in the accrual of Tom$^+$ cells was observed in *Tet2*$^{fl/fl}$ reporter mice versus controls (Fig. S2 A). Similarly, no accelerated accrual of Tom$^+$ cells was observed in aged (18-mo-old) *Tet2*$^{fl/fl}$ reporter mice (Fig. S2 B), which showed the same global reduction of multilineage HSC contribution as WT reporters (Jang et al., 2023) (Fig. S2, C–F). The recombined *Tet2*^{fl} allele was predominant in the Tom$^+$ fraction of total BM cells in both homozygous *Tet2*$^{fl/fl}$ and heterozygous *Tet2*$^{fl/wt}$ reporter mice at 6 mo after induction (Fig. S2, G and H). However, the recombined allele was also clearly detectable in the Tom$^-$ fraction, and the difference between Tom$^+$ and Tom$^-$ fractions was not as strong as for *Kras*^{G12D}, possibly due to the extended timeframe of tracing.

Because the injection of microbial mimic Pam3CSK4 facilitates myeloproliferation in mice with global *Tet2* deletion (Meisel et al., 2018), *Tet2*$^{fl/fl}$ or WT reporter mice were administered tamoxifen together with 3 daily doses of Pam3CSK4 (Fig. S3 A). Pam3CSK4-treated *Tet2*$^{fl/fl}$ reporter mice showed no consistent increase in Tom$^+$ cells in the PB over 6 mo compared with untreated *Tet2*$^{fl/fl}$ mice, likely due to the high labeling variability in the latter (Fig. S3 B). However, compared with Pam3CSK4-treated WT reporter mice, Pam3CSK4-treated *Tet2*$^{fl/fl}$ mice showed a significant increase of Tom$^+$ cells in platelets (at 1–6 mo) and in myeloid cells (at 4–6 mo). This increased labeling was confirmed in myeloid cells at the 6-mo endpoint (Fig. S3 C) and was also evident in MPP and myeloid progenitors (MyP) (Fig. S3, D and E). As noted above, the tracing of Tet2-deficient cells may underestimate their expansion in the Tom$^-$ fraction. Even with this caveat, the data suggest that ARCH-associated mutations such as *Tet2* deletion have a smaller effect on HSC contribution than Kras activation, but can modestly enhance it following inflammatory stimulation.

Kras^{G12D} mutation in HSC generates hypercompetitive multilineage progenitors

We sought to map the stage at which the expansion of Kras-mutant cells is commenced following Kras activation in HSC. At 2 wk, the fractions of Tom$^+$ stem/progenitor cells were comparable between *Kras*^{G12D} and WT reporter mice (Fig. 2 A). At 3 wk, *Kras*^{G12D} reporter mice showed increased fractions of Tom$^+$ cells among erythroid progenitors (EryP) and MyP. Tom$^+$ cells were also increased among Flt3$^-$ MPP (MPP3) and Flt3$^+$ MPP (MPP4 [Pietras et al., 2015]), albeit not reaching significance in the former. At 5 wk, Tom$^+$ cells among MPP3, MPP4, and all downstream progenitors were significantly increased, approaching the level of HSC labeling (Fig. 2 A) and exceeding it by 7 wk (Fig. S1 G). Similarly, labeled MPP (hereafter representing combined MPP3 and MPP4), EryP, and MyP were significantly increased in absolute numbers at 3 and 5 wk in *Kras*^{G12D} reporter mice (Fig. 2 B). In contrast, Tom$^+$ HSC and ST-HSC were not increased at any point and even showed a minor decrease at 3 wk, suggesting that the expansion of *Kras*-mutant cells commences at the MPP stage.

The analysis of Tom$^+$ cells among IL-7R$^+$ lymphoid progenitors (LyP) in *Kras*^{G12D} reporter mice revealed a widespread upregulation of IL-7R among all Flt3$^+$ progenitors. These included Sca-1$^-$ c-Kit$^-$ and c-Kit$^{lo/int}$ progenitors harboring the so-called common LyP, as well as Sca-1$^-$ c-Kit$^+$ MyP and Sca-1$^+$ c-Kit$^+$ MPP4 (Fig. 2, C–E). Importantly, Tom$^+$ cells were dramatically expanded among IL-7R$^+$ cells in all these populations at 3 wk after induction in *Kras*^{G12D} reporter mice (Fig. 2 F). These data are consistent with the induction of IL-7R expression by the Ras signaling pathway (Li et al., 2010) and reveal widespread lymphoid priming of mutant progenitors starting from the MPP4 stage.

We measured the proliferation rate of stem/progenitor populations by injecting mice with 1 mg 5-ethynyl-2′-deoxyuridine (EdU) and detecting its incorporation 2 h later by flow

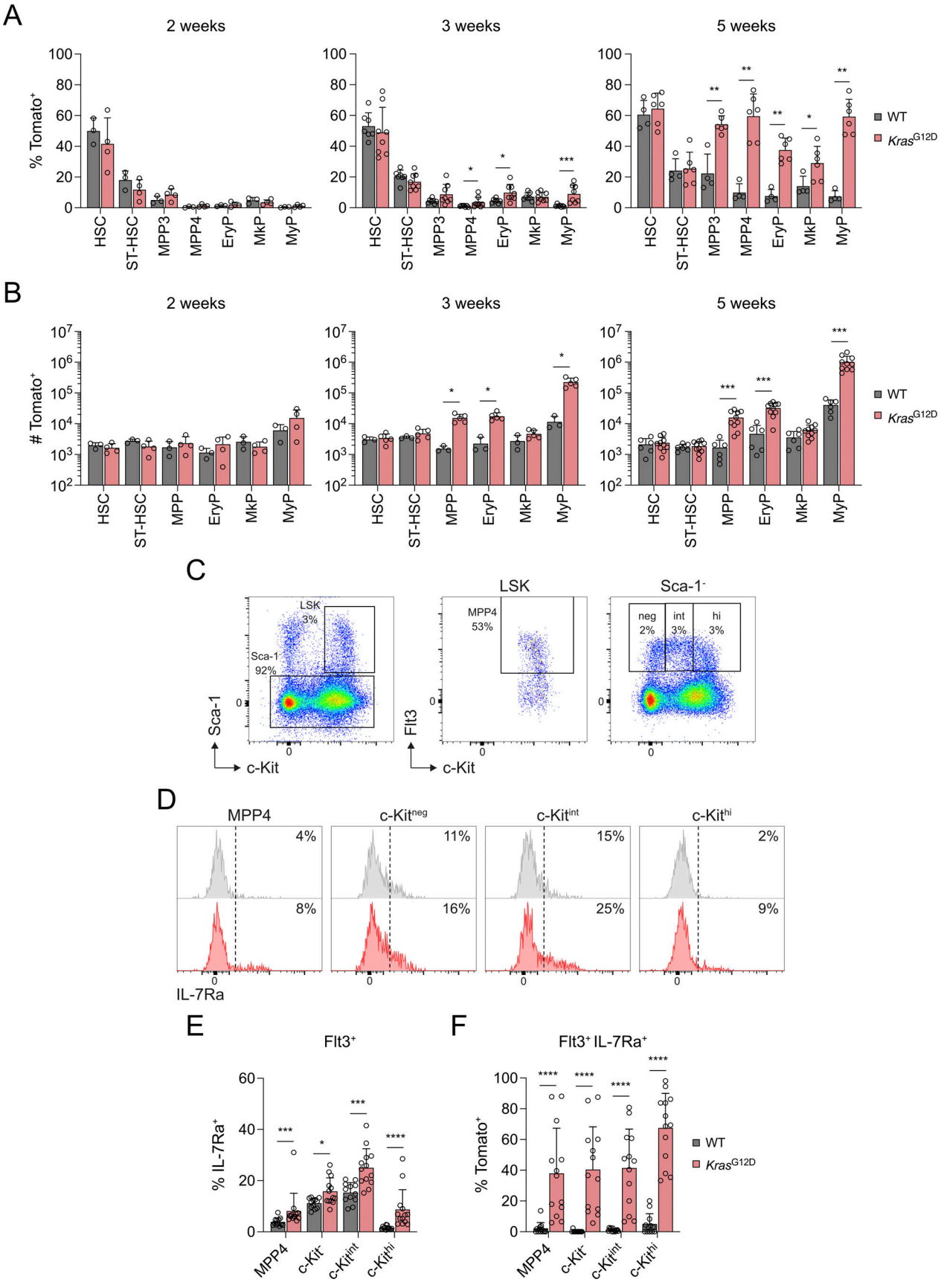

Figure 2. ***Kras*^{G12D} mutation in HSC causes expansion of multipotent and lymphoid-primed progenitors.** *Pdzk1ip1*-CreER *R26*$^{Tom/Tom}$ reporter mice with WT or conditional mutant (*Kras*^{G12D}) *Kras* alleles were administered tamoxifen to induce simultaneous Tom expression and *Kras* mutation in HSC. Stem/

progenitor populations in the BM were analyzed at the indicated time points after tamoxifen treatment. **(A)** Fractions of Tom$^+$ stem/progenitor cell populations. Symbols represent individual mice; bars represent the mean ± SD of data from a single experiment (2 and 5 wk) or from two experiments (3 wk). **(B)** Absolute numbers of Tom$^+$ stem/progenitor cell populations. Symbols represent individual mice; bars represent the mean ± SD of data from a single experiment (2 and 3 wk) or from two experiments (5 wk). The data correspond to (2 wk) or partially overlap (3 and 5 wk) those in panel A. **(C–F)** Expression of IL-7R on Flt3$^+$ progenitors in WT or *Kras*^{G12D} reporter mice at 3 wk after tamoxifen administration. **(C)** Representative staining of the Lin$^-$ population from a *Kras*^{G12D} reporter mouse, highlighting Flt3$^+$ MPP4 within the gated LSK cells, and Flt3$^+$ cells with negative (neg), intermediate (int), or high (hi) levels of c-Kit within the gated Sca-1$^-$ cells. **(D)** Representative histograms of IL-7R expression on total Flt3$^+$ progenitors defined in panel C from WT (gray, top row) or *Kras*^{G12D} (red, bottom row) reporter mice. **(E)** Fraction of IL-7R$^+$ cells among the total gated Flt3$^+$ progenitors in WT or *Kras*^{G12D} reporter mice. **(F)** Fraction of Tom$^+$ cells among the gated Flt3$^+$ IL-7R$^+$ progenitors in WT or *Kras*^{G12D} reporter mice. In panels E and F, symbols represent individual mice; bars represent the mean ± SD of data from two experiments. Statistical significance was estimated by the Mann–Whitney test. *P < 0.05, **P < 0.01, ***P < 0.001, ****P < 0.0001.

cytometry (Akinduro et al., 2018). We compared the fractions of EdU$^+$ cells in Tom$^+$ and Tom$^-$ cell fractions in *Kras*^{G12D} reporter mice 5 wk after tamoxifen treatment, as well as in total cells in WT reporter mice (given the low fraction of Tom$^+$ cells at that stage) (Fig. 3 A). As expected, HSC and ST-HSC showed low but detectable EdU incorporation, which was progressively increased in MPP and erythromyeloid progenitors in WT mice (Fig. 3 B). Notably, only Tom$^+$ MPP showed a significantly increased EdU incorporation in *Kras*^{G12D} reporter mice when compared both to Tom$^-$ counterparts from the same mice and to the same population from WT mice (Fig. 3 B). This significant increase was observed in both MPP3 and MPP4 analyzed separately (Fig. 3 C). Moreover, a similar increase in EdU incorporation in MPP (but not in HSC) was observed at 3 wk, the earliest time point of Tom$^+$ cell expansion in *Kras*^{G12D} reporter mice (Fig. 3 D). We repeated these experiments at 3 wk after induction using two injections of 1 mg EdU over the 48-h period and stained cells for EdU incorporation along with DNA content. Again, HSC and ST-HSC showed minimal differences between Tom$^+$ and Tom$^-$ cell fractions in *Kras*^{G12D} reporter mice or total cells in WT reporter mice (Fig. 3 E). In contrast, MPP showed a significant increase in EdU$^+$ cells and a reciprocal decrease in EdU$^-$ 2n cells, i.e., cells that did not enter the S-phase within 48 h (Fig. 3, F and G). These data suggest that the induction of *Kras*^{G12D} in HSC does not affect their proliferation rate, but increases that of the downstream MPP population.

To test whether this increased proliferation rate reflected the acquisition of self-renewal capacity, we sorted Tom$^+$ HSC or MPP from *Kras*^{G12D} reporter mice 5 wk after tamoxifen treatment and transferred them into lethally irradiated CD45.1 congenic recipients along with supporting total CD45.1 BM cells. Whereas the transfer of 50 HSC/recipient resulted in durable multilineage reconstitution by CD45.2$^+$ donor cells, the transfer of 1,000 MPP/recipient yielded a small fraction of donor-derived lymphocytes at 1 mo, and no detectable reconstitution thereafter (Fig. 3 H). Thus, Kras activation in HSC causes a rapid expansion of mutant MPP, which show increased proliferation but are incapable of self-renewal.

Kras^{G12D}-expressing MPP have a distinct transcriptome

To characterize the *Kras*^{G12D}-carrying HSC and their immediate progeny, we analyzed them by cellular indexing of transcriptomes and epitopes (CITE-seq). CITE-seq enables combined single-cell RNA sequencing of multiple samples by labeling them using oligonucleotide-conjugated antibody "hashtags" (Stoeckius et al., 2018). *Pdzklip1*-CreER *R26*$^{Tom/Tom}$ *Kras*^{G12D} or WT reporter mice were treated with tamoxifen and analyzed at 3 wk, the earliest time point for the expansion of Kras-mutant progenitors. Lin$^-$ BM cells were isolated, hashtagged, and used to sort the LSK population. For *Kras*^{G12D} reporter mice, Tom$^+$ LSK cells were sorted; because WT reporter mice have very few Tom$^+$ MPP at this time point (Fig. 2 A), total LSK cells were sorted (Fig. 4 A). Hashtagged LSK cells from two individual mice per genotype were pooled and subjected to sequencing. Because the standard Uniform Manifold Approximation and Projection could not fully resolve the closely related HSC and MPP (Fig. S4 A), we applied K-nearest neighbor-based Network graph drawing Layout (KNetL) (Feng et al., 2022; Khodadadi-Jamayran and Tsirigos, 2020, *Preprint*) to yield nine distinct clusters (Fig. S4 B). One of these clusters (cluster 3) represented contaminating mature cells including MHC class II–expressing dendritic cells (Fig. S4 C and Table S1) and was removed, whereas two closely related clusters (clusters 2 and 6) were merged, yielding seven final clusters (Fig. 4 B). Based on the expression of characteristic marker genes (Fig. 4 C and Table S1), the clusters were identified as HSC (cluster 1), three clusters of MPP (clusters 2&6, 4, and 5), an additional cluster of MPP with a strong proliferation signature (prolif. MPP, cluster 9), MyP (cluster 7), and megakaryocyte/erythroid progenitors (MEP, cluster 8).

The majority of cells in the resulting dataset (10,594 cells) were derived from one *Kras*^{G12D} mouse (3,472 cells) and two WT mice (2,829 and 3,461 cells) (Fig. 4 D). The contributions of individual *Kras*^{G12D} and WT mice to the HSC cluster 1 were comparable to the entire dataset (Fig. 4 D), suggesting a similarity of *Kras*^{G12D} and WT HSC transcriptomes. However, MPP clusters 2&6 and 4 were comprised predominantly WT and Kras-mutant cells, respectively (Fig. 4 D). Accordingly, pairwise comparison between WT and Kras cells within the HSC cluster showed minimal differences, with only 6 differentially expressed genes (DEG) showing a greater than twofold difference with statistical significance (adjusted P value <0.05) (Fig. 4 E and Table S2). These included the upregulation of Ras targets *Junb* and *Egr1* and downregulation of the differentiation marker *Cd52* (Fig. S4 D and Table S2). In contrast, MPP clusters showed 758 significant DEG (Fig. 4 E and Table S2), which included downregulation of many HSC-related genes (e.g., *Meis*, *Tal1*, *Pbx1*, *Mpl*, *Pdzklip1*) in mutant MPP (Fig. S4 D). Conversely, mutant MPP showed the upregulation of lymphoid development–associated genes (sterile *Ighv* transcripts, *Rag2*, *Ccr9*, *Ebf1*, *Dntt*) and downregulation of *Dach1*, a negative marker of LyP (Amann-Zalcenstein et al., 2020) (Fig.

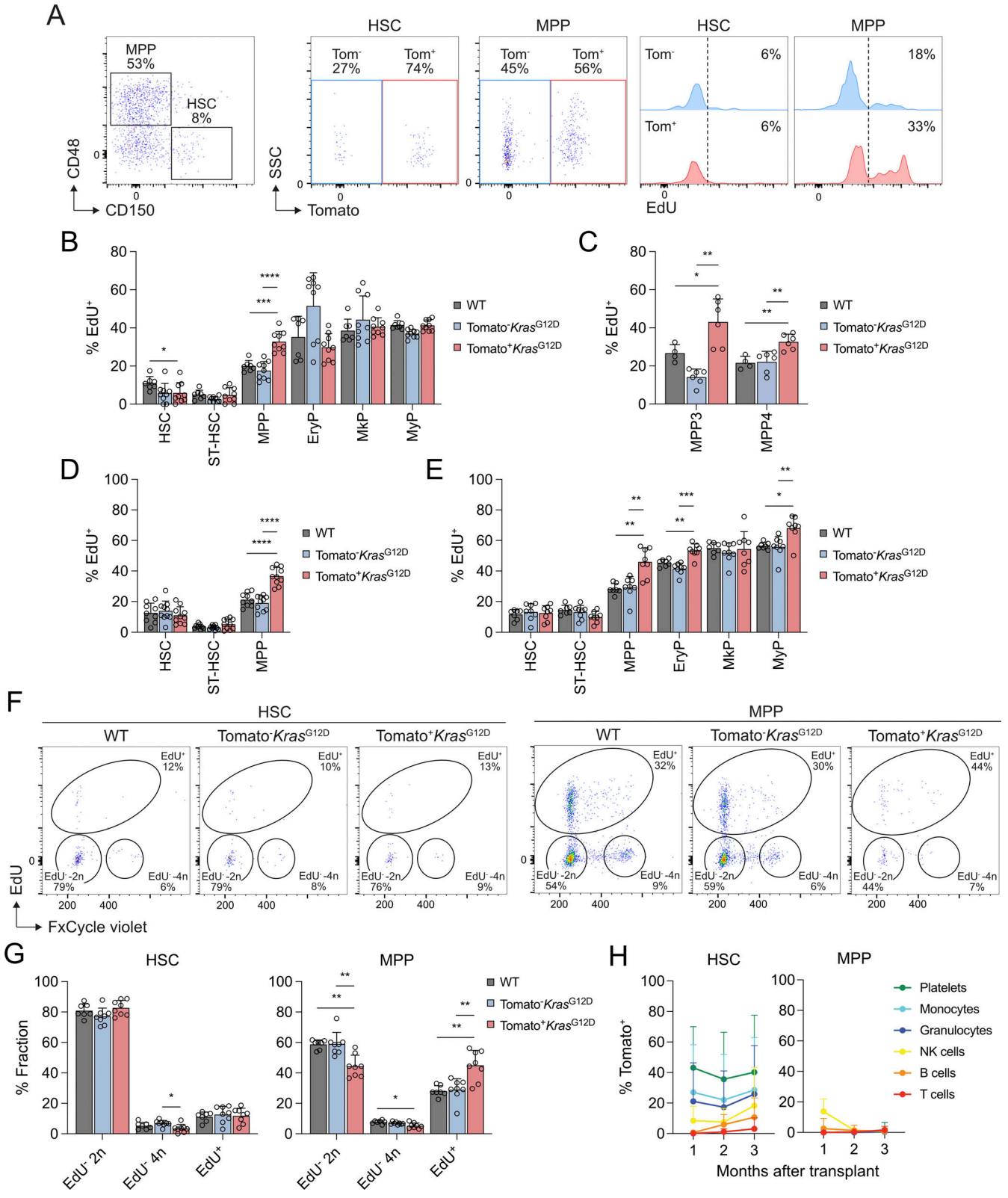

Figure 3. ***Kras^G12D*-carrying MPP show increased proliferation but lack self-renewal. (A–G)** *Pdzk1ip1*-CreER *R26*$^{Tom/Tom}$ reporter mice with WT or conditional mutant (*Kras*^{G12D}) *Kras* alleles were administered tamoxifen to induce simultaneous Tom expression and *Kras* mutation in HSC. At the indicated time points after tamoxifen treatment, mice were injected i.p. with EdU, and EdU incorporation in the stem/progenitor populations in the BM was measured by flow cytometry. **(A–C)** Mice at 5 wk after tamoxifen treatment were injected with EdU and analyzed 2 h later. **(A)** Representative staining profiles of gated LSK cells from *Kras*^{G12D} mice, showing EdU staining within gated Tom⁻ (blue) and Tom⁺ (red) HSC and MPP. **(B)** Fraction of EdU⁺ cells in the Tom⁺ (red) or Tom⁻ (blue) subset within the indicated populations from *Kras*^{G12D} reporter mice. Total stem/progenitor populations from WT mice were used as controls (gray) due to

minimal Tom labeling of progenitors at this time point. Symbols represent individual mice; bars represent the mean ± SD of data pooled from two independent experiments. **(C)** Fraction of EdU$^+$ cells in MPP3 and MPP4 subsets determined as above (data from a single experiment). **(D)** Mice at 3 wk after tamoxifen treatment were injected with EdU and analyzed 2 h later. The fraction of EdU$^+$ cells in HSC and MPP is shown as above (data pooled from two independent experiments). **(E–G)** Mice at 3 wk after tamoxifen treatment were injected with EdU twice daily and analyzed 48 h after the first injection. **(F)** Representative staining profiles of gated HSC or MPP from WT (total cells) or *Kras*^{G12D} (Tom$^+$ or Tom$^-$ cells) mice, showing staining for EdU and DNA content. Total EdU$^+$ cells or EdU$^-$ cells with 2n or 4n DNA content are indicated. **(G)** Fractions of EdU$^+$, EdU$^-$ 2n, or EdU$^-$ 4n populations among gated HSC or MPP shown as in panels B–E (data from a single experiment). **(H)** Reconstitution capacity of *Kras*^{G12D} MPP. *Kras*^{G12D} reporter mice were administered tamoxifen, and their BM was isolated 5 wk later. Tom$^+$ HSC (50 cells) or Tom$^+$ MPP (1,000 cells) were mixed with 2 × 10^5 total BM from CD45.1 congenic mice and transferred into lethally irradiated CD45.1 recipients. Two donor mice were induced, and donor cells from each mouse were transferred separately. The accrual of Tom$^+$ donor-derived cells was measured in the PB at the indicated time points. Symbols represent the mean ± SD of the recipients of HSC (n = 7) or of MPP (n = 13). Statistical significance was estimated by the Mann–Whitney test. *P < 0.05, **P < 0.01, ***P < 0.001, ****P < 0.0001.

S4, D and E; and Table S2). Many genes associated with proliferation (e.g., *Ccna2*, *Cdca8*, *Cenpw*, *Mcm10*, *Cdk1*) were also upregulated in mutant MPP (Fig. S4, D and F; and Table S2). The extent of differential expression was lower in proliferative MPP (400 DEG), although the same patterns were observed (e.g., downregulation of *Pbx1*, *Mpl*, and *Dach1*, and upregulation of *Ighv* and *Rag2*) (Fig. 4 E and Table S2). On the other hand, much less differential expression was observed in MEP (99 DEG) and MyP (18 DEG) (Fig. 4 E and Table S2). Collectively, these data support the notion that Kras mutation has a minimal effect on the transcriptome of HSC, but strongly affects the transcriptome of mutant MPP, which show enhanced differentiation, lymphoid priming, and proliferation.

Osteopontin facilitates the early stages of Kras-mutant progenitor expansion

The rapid takeover of the MPP population by Kras-mutant cells raised the possibility that they outcompete normal cells by mechanisms beyond increased proliferation. We noted that the Kras-specific MPP cluster showed the increased expression of *Tnf* (encoding the inflammatory cytokine TNF-α) and *Spp1* (encoding osteopontin) (Fig. S4 D and Fig. 5 A). Osteopontin is a secreted glycoprotein that is produced by stromal cells and restricts the size of the normal HSC and progenitor pool (Grassinger et al., 2009; Stier et al., 2005). To test its potential role in the expansion of mutant MPP, we crossed *Pdzklip1*-CreER *R26*^{Tom} WT or *Kras*^{G12D} mice onto the osteopontin-null (*Spp1*$^{-/-}$) background.

First, we tested the contribution of normal HSC in *Pdzklip1*-CreER *R26*^{Tom} *Spp1*$^{-/-}$ or control *Spp1*$^{+/+}$ mice without the *Kras*^{G12D} allele. Given the relatively slow labeling of normal progenitors in WT reporter mice, we analyzed Tom$^+$ cells 12 wk after tamoxifen administration. The initial labeling of HSC was comparable between *Spp1*$^{-/-}$ and *Spp1*$^{+/+}$ mice as determined by BM biopsy (Fig. S5 A). At the endpoint, we observed a comparable labeling of HSC and a minor <1.5-fold reduction in the labeling of downstream populations in *Spp1*$^{-/-}$ reporter mice. The reduction reached statistical significance in B cells and their progenitors, and in some additional progenitor populations (megakaryocyte progenitors [MkP], MyP, DN2/3, and DP thymocytes) but not in MPP or in mature myeloid cells (Fig. S5, B–E). We then analyzed tamoxifen-induced *Kras*^{G12D} reporter mice that were *Spp1*$^{+/+}$ or *Spp1*$^{-/-}$, which also showed comparable HSC labeling at the start of tracing (Fig. S5 F). Subsequent tracing revealed the expected acceleration of label accrual in *Kras*^{G12D} mice that was comparable between *Spp1*$^{+/+}$ and *Spp1*$^{-/-}$ reporters at the 7-wk endpoint (Fig. S5, G–J). Thus, osteopontin has a minor effect on the steady-state differentiation of normal HSC and is dispensable for the long-term expansion of Kras-mutant cells.

We then tested an earlier role of osteopontin by examining the *Kras*^{G12D} reporter mice at 3 wk after labeling, when the expansion of Kras-mutant cells first becomes apparent. We observed a highly significant reduction of Tom$^+$ cells in all mature cells, in all stages of B-cell development in the BM, and in the thymic ETP of *Spp1*$^{-/-}$ reporter mice (Fig. 5, B–D). We also observed a modest less than twofold reduction in the fraction of Tom$^+$ HSC, potentially suggesting some effect of osteopontin on the maintenance of mutant HSC (Fig. 5 E). Irrespectively, the reduction in the labeling of all downstream progenitors was much more pronounced, suggesting its key role in the reduced labeling of mature cells (Fig. 5 E). Of note, these experiments could not establish the relevant source of osteopontin, which may be derived from mutant MPP, from stromal cells, or both; nor did they identify the specific stage of differentiation affected by osteopontin. Nevertheless, these results suggest a role of osteopontin in the initial expansion of *Kras*-mutant progenitors, possibly by favoring them over normal progenitors.

Kras^{G12D}-expressing stem/progenitor cells show enhanced motility

We sought to define additional mechanisms whereby mutation-carrying progenitors outcompete their normal counterparts. Stem and progenitor cells in their BM niche display CXCR4-dependent motility that facilitates their retention in the BM and the interaction with stroma (Beck et al., 2014; Upadhaya et al., 2020). To analyze the behavior of Kras-mutant cells in their BM niche, we examined *Pdzklip1*-CreER *R26*^{Tom} *Kras*^{G12D} or WT mice 2–3 wk after tamoxifen treatment by two-photon laser scanning microscopy (Fig. 6 A). We thinned the bone wall of tibiae in anesthetized mice and imaged the underlying BM continuously for 60 min with a frame rate of 45–55 s. HSC and their progeny were defined as Tom$^+$ and distinguished from autofluorescent macrophages (Upadhaya et al., 2020) (Fig. 6 B, Video 1, and Video 2). At 2–3 wk after tamoxifen treatment, Tom$^+$ cells comprise a mixture of HSC, various progenitors, and some Lin$^+$ cells; thus, HSC and MPP cannot be distinguished by this method. Notably, the composition of Tom$^+$ cells is comparable between *Kras*^{G12D} and WT reporter mice at 2 wk (Fig. 2, A and B). We found that labeled cells in

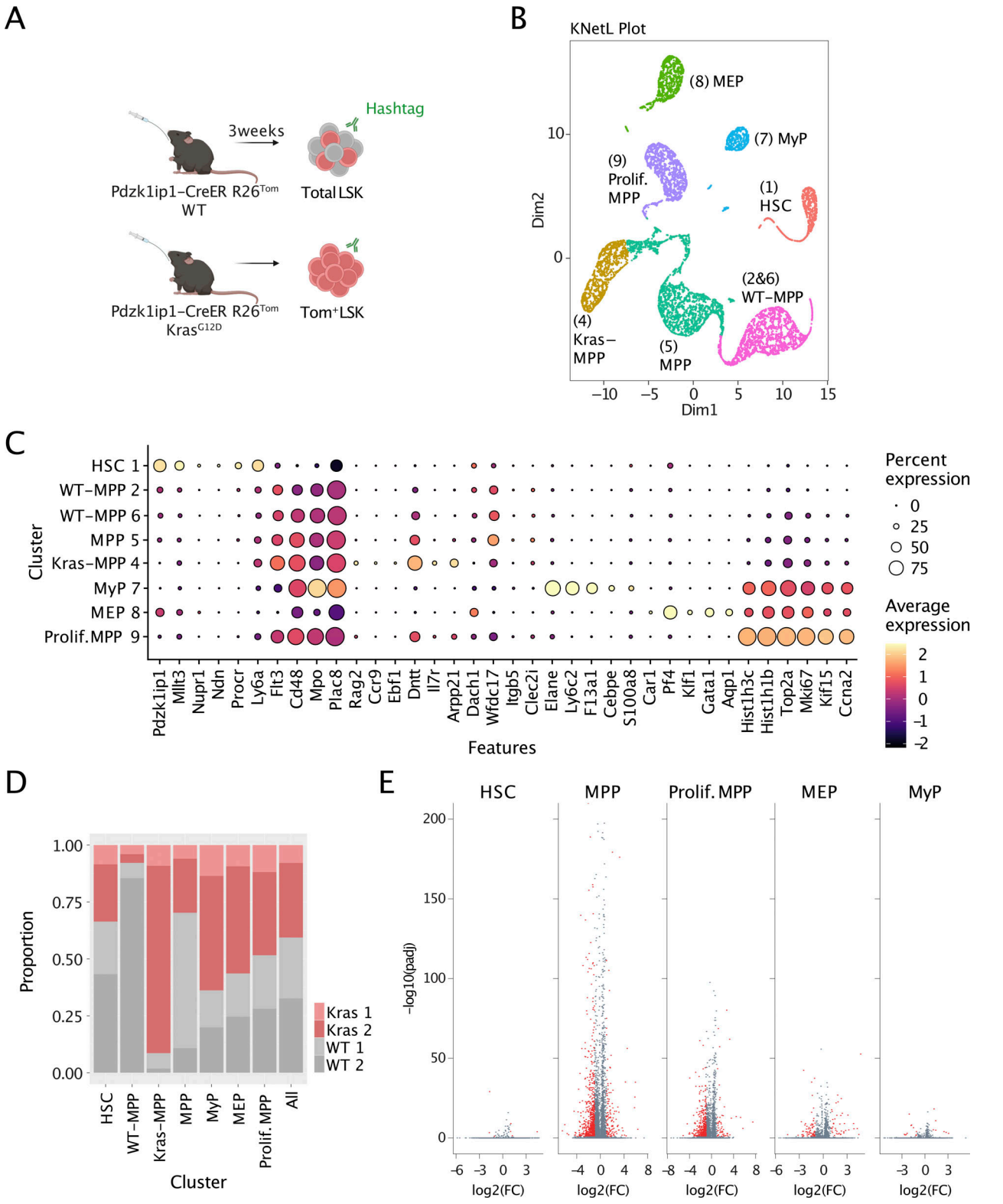

Figure 4. ***Kras*^{G12D} mutation–carrying MPP have distinct transcriptomes. (A)** CITE-seq analysis of Kras-mutant stem/progenitor cells. *Pdzk1ip1*-CreER *R26*$^{Tom/Tom}$ *Kras*^{G12D} or WT reporter mice were induced with tamoxifen. 3 wk later, hashtagged Tom$^+$ LSK from *Kras*^{G12D} reporters or total LSK from WT reporters were sorted separately from two individual mice per group, pooled, and analyzed by CITE-seq. **(B)** KNetL plot of single cells clustered by transcriptomic data. Resulting clusters are indicated by color and labeled with their proposed identity. **(C)** Dot plots of marker gene expression in the clusters shown in panel B. **(D)** Fractions of individual samples within each cluster, as well as among all cells. **(E)** Pairwise comparison of gene expression between *Kras*^{G12D} and WT cells within each respective cluster (for HSC, prolif. MPP, MEP, and MyP) or combined WT-MPP and Kras-MPP clusters (for MPP). Shown are volcano plots with dots corresponding to individual genes; those with significant differential expression are highlighted in red. FC, fold change.

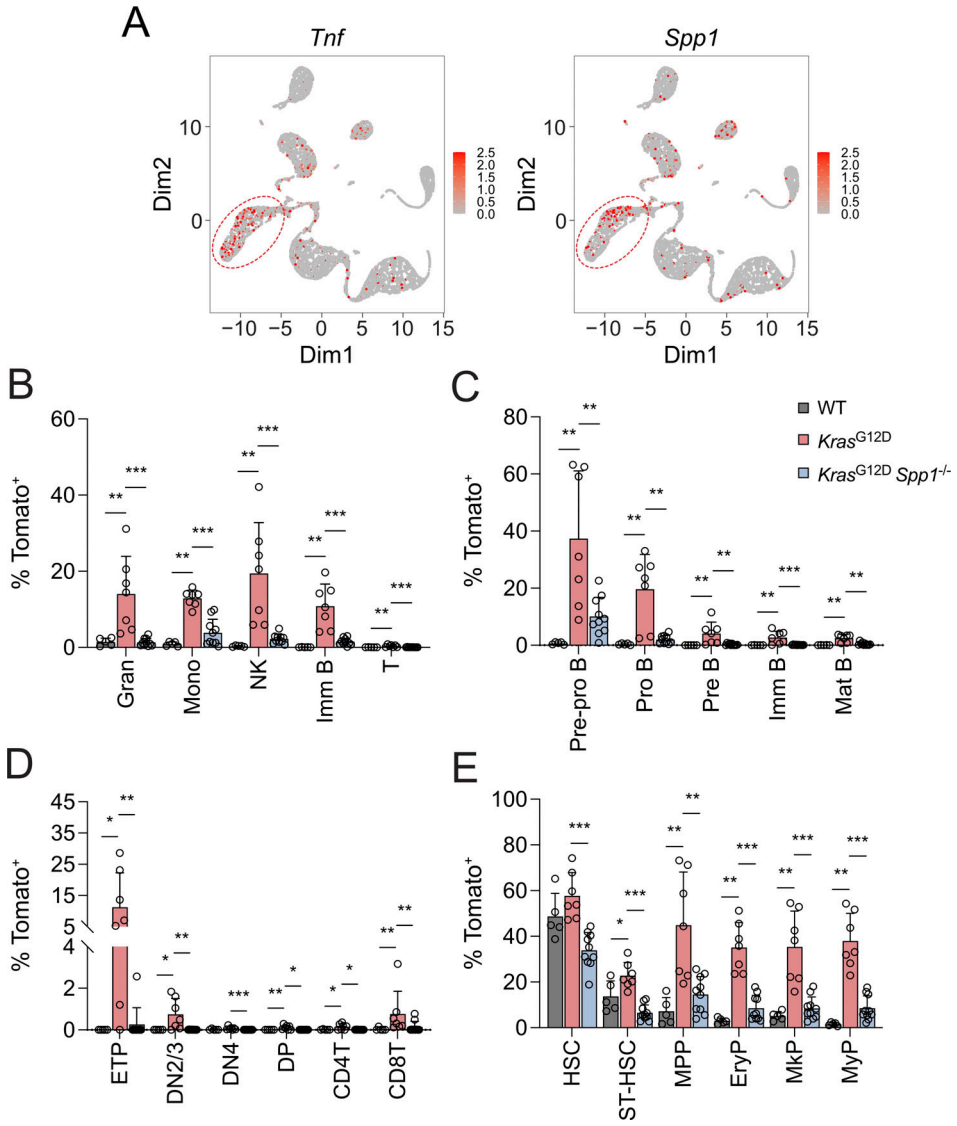

Figure 5. **Contribution of *Kras*^{G12D}-mutant HSC is delayed by osteopontin deficiency. (A)** Feature plots showing the expression of *Tnf* (encoding TNF-α) or *Spp1* (encoding osteopontin) in individual cells on the KNetL plot (Fig. 4). The *Kras*^{G12D}-specific MPP cluster is highlighted. **(B–E)** Contribution of *Kras*^{G12D}-mutant HSC with or without osteopontin. HSC-specific Cre reporter mice (*Pdzk1ip1*-CreER *R26*$^{Tom/Tom}$) that carried WT *Kras* allele, a conditional mutant (*Kras*^{G12D}) *Kras* allele alone, or *Kras*^{G12D} allele with a germline deletion of *Spp1* (*Spp1*$^{-/-}$) were administered a single dose of tamoxifen to induce simultaneous Tom expression and *Kras* mutation in HSC, and analyzed at the 3-wk endpoint. Shown is the fraction of Tom$^+$ cells within mature BM cell types (B), subsets of B cells in the BM (C), and subsets of thymocytes (D) and stem/progenitors in the BM (E). Symbols represent individual mice; bars represent the mean ± SD; data are pooled from two independent experiments. Statistical significance was estimated by the Mann–Whitney test. *P < 0.05, **P < 0.01, ***P < 0.001.

Kras^{G12D} reporter mice showed higher motility as defined by track reconstruction in the *xy* plane (Fig. 6, B and C), track and displacement velocities (Fig. 6 D), and mean squared displacement (MSD [Fooksman et al., 2010]) over time (Fig. 6 E). Critically, all these differences were significant both at 3 and at 2 wk.

To model the increased motility of Kras-mutant progenitor cells in vitro, we tested Lin$^-$ BM cells from *Kras*^{G12D} or WT reporter mice in a transwell migration assay toward the CXCR4 ligand CXCL12 (Fig. 6 F). Cells were additionally enriched for MPP by depletion with antibodies against CD11c, CD115, CD16/32, and CD41. Tom$^+$ cells showed lower migration than Tom$^-$ cells in WT mice, likely because they comprise HSC and early progenitors that are less mobile in vitro than the more differentiated Tom$^-$ cells. Importantly, Tom$^+$ cells from *Kras*^{G12D} mice showed enhanced migration toward CXCL12, whereas the migration of Tom$^-$ cells was similar to WT (Fig. 6 G). Accordingly, we found that the expression of CXCR4 was significantly increased on Tom$^+$ MPP but not on HSC from *Kras*^{G12D} mice (Fig. 6, H and I). Collectively, these results suggest that Kras-mutant cells show increased motility in their BM niche in vivo; moreover, MPP-enriched cells show increased CXCR4-dependent migration in vitro, corresponding to the increased CXCR4 expression on MPP.

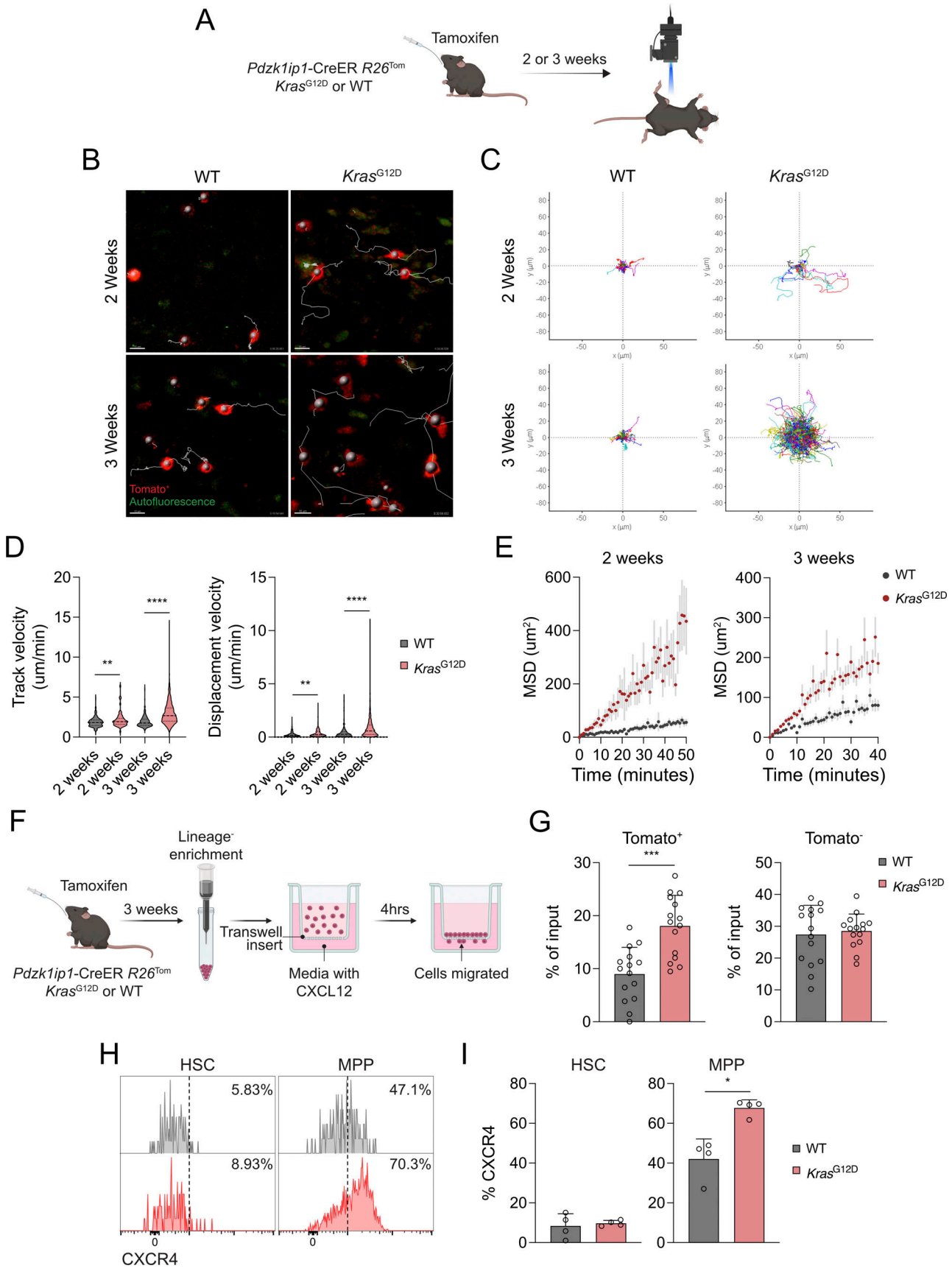

Figure 6. ***Kras*^{G12D} mutation–carrying BM cells show increased motility in vivo. (A)** Analysis of *Kras*-mutant cell behavior in vivo. *Pdzk1ip1*-CreER *R26*$^{Tom/Tom}$ reporter mice with WT or conditional mutant (*Kras*^{G12D}) *Kras* alleles were administered tamoxifen to induce simultaneous Tom expression and

Kras mutation in HSC. 2 or 3 wk later, their tibiae were examined by intravital microscopy using continuous frame recording for 1 h. **(B)** Representative snapshots of intravital imaging of reporter mice at the indicated time points. Red and green signals represent Tom+ cells and autofluorescent macrophages, respectively; select Tom+ cells are marked by gray spheres, and their tracks are indicated. Data are representative of three to four mice per group per time point. Scale bar, 10 µm. **(C)** Representative flower plots showing tracks of individual Tom+ cells (marked by different colors) relative to each cell's starting point. **(D and E)** Motility of Tom+ cells. Shown are violin plots of track velocity and displacement velocity of individual Tom+ *Kras*^{G12D} or WT cells at 2 or 3 wk (D) and their corresponding MSD (E). For the 2-wk experiment, individual Tom+ WT cells (109 cells from four mice) and Tom+ *Kras*-mutant cells (40 cells from four mice) were analyzed. For the 3-wk experiment, individual Tom+ WT cells (206 cells from four mice) and Tom+ *Kras*-mutant cells (677 cells from three mice) were analyzed. Lines on violin plots indicate median and quartiles; on MSD graphs, symbols indicate mean MSD values for all tracks at the indicated time point and ranges indicate the standard error. **(F and G)** CXCL12-driven migration of Tom+ cells in vitro. **(F)** Lin− cells were isolated by magnetic negative selection using additional depletion of committed progenitors by antibodies to CD11c, CD115, CD16/32, and CD41. The resulting cells from reporter mice 3 wk after tamoxifen treatment were used in a transwell migration assay toward CXCL12 for 4 h. **(G)** Fractions of Tom+ or Tom− Lineage− cells that migrated into the bottom chamber. Symbols represent individual transwell cultures seeded in triplicates from five mice per genotype pooled from two independent experiments. **(H and I)** Expression of CXCR4 in Kras-mutant stem/progenitor cells. **(H)** Representative histograms of CXCR4 staining in Tom+-gated HSC or MPP from *Kras*^{G12D} or WT reporter mice 3 wk after induction. The threshold of positive staining is indicated by the dotted line. **(I)** Fractions of CXCR4+ cells in Tom+ HSC or MPP, and MFI of CXCR4 in MPP. Symbols represent individual mice; bars represent the mean ± SD Statistical significance was estimated by unpaired Student's *t* test (D) or the Mann–Whitney test (other panels). *P < 0.05, **P < 0.01, ***P < 0.001, ****P < 0.0001. MFI, mean fluorescence intensities.

CXCR4-dependent motility of Kras-mutant progenitors contributes to their expansion in vivo

To prove that the increased in vivo motility of Kras-mutant progenitors is driven by CXCR4, we used LY2510924, a potent selective peptide antagonist of CXCR4 (Peng et al., 2015). We imaged Tom+ stem/progenitor cells in live tamoxifen-induced *Kras*^{G12D} or WT reporter mice for 60 min as above, administered LY2510924 i.v., and continued the imaging for an additional 60 min. After LY2510924 administration to WT reporter mice, Tom+ cells rounded up and ceased to move (Video 3 and Fig. 7 A). The same change of morphology and reduction of motility were observed in Tom+ cells from *Kras*^{G12D} mice, although not to the level of WT mice (Video 4 and Fig. 7 A). The reduced motility of Tom+ cells after LY2510924 administration in both *Kras*^{G12D} and WT reporter mice was evident from shortened tracks (Fig. 7 B), reduced track and displacement velocities (Fig. 6 C), and reduced MSD of Tom+ cells (Fig. 7 D). Thus, LY2510924 blocks CXCR4 and reduces the motility of Kras-mutant cells in the BM.

To test whether CXCR4 blockade affects the rapid expansion of Kras-mutant cells from MPP in vivo, *Kras*^{G12D} or WT reporter mice at 2 wk after tamoxifen treatment were treated with LY2510924 or with vehicle (PBS) for 1 wk and analyzed at the 3-wk endpoint (Fig. 7 E). As expected, HSC labeling was similar between *Kras*^{G12D} and WT mice and was unaffected by the treatment (Fig. 7 F). However, the highly elevated labeling of MPP and downstream progenitors in *Kras*^{G12D} reporters was significantly reduced by LY2510924 (Fig. 7 F). Furthermore, the inhibitor significantly reduced the labeling of mature cells in the spleen of treated *Kras*^{G12D} reporter mice (Fig. 7 G). A similar trend (albeit with higher variability) was observed in the BM (Fig. 7 H). Thus, CXCR4 mediates the increased motility of Kras-mutant progenitors in the BM and contributes to their rapid expansion in vivo.

Kras-targeted therapy abolishes the expansion of mutant cells but spares their HSC reservoir

Our data suggest that HSC serve as a reservoir of the *Kras*^{G12D} mutation, which rapidly spreads to multiple lineages via hypercompetitive progenitors. To test whether the chemical inhibition of mutant KRAS may impair the maintenance or spread of the mutation, we first used a combination therapy with mirdametinib (PD0325901) and pictilisib (GDC-0941). These small molecules inhibit RAS-activated MEK/ERK and PI(3)K signaling pathways, respectively, and have shown efficiency against *Kras*^{G12D}-driven leukemia (Dail et al., 2014). 2 wk after tamoxifen induction, *Pdzklip1*-CreER *R26*$^{Tom/Tom}$ WT or *Kras*^{G12D} mice were treated daily with PD0325901 and GDC-0941 for 4 days followed by GDC-0941 alone for 3 days, and the fraction of *Kras*-mutant Tom+ cells was examined in the spleen and BM (Fig. 8 A). In this experiment, the fraction of Tom+ HSC showed a significant ∼1.3-fold expansion in untreated *Kras*^{G12D} versus WT reporter mice, and this expansion was abolished by the treatment (Fig. 8 B). However, Tom+ MPP and erythromyeloid progenitors showed the expected >10-fold expansion in *Kras*^{G12D} reporters, and this expansion was reduced ∼2-fold and ∼4-fold, respectively (Fig. 8 B). Accordingly, the expansion of Tom+ cells within mature splenic myeloid and lymphoid lineages of treated *Kras*^{G12D} reporter mice was reduced three- to fourfold, reaching significance in granulocytes, monocytes, and T cells (Fig. 8 C). The minor reduction of mutant HSC is unlikely to contribute to the effect, because (1) HSC contribution to differentiation is extremely low at this early time point (Upadhaya et al., 2018); and (2) only MPP and downstream progenitors underwent a major expansion commensurate with that of mature cells (Fig. 8, B and C).

To directly target the driver mutation, we used a recently developed small molecule inhibitor of the mutant KRAS^{G12D} protein, MRTX1133. Unlike PD0325901/GDC-0941, MRTX1133 targets the mutation itself rather than its downstream pathways, exhibits a >1,000-fold selectivity for KRAS^{G12D}-expressing versus KRAS^{WT} cells, and does not have any off-target effects at therapeutic concentrations used herein (Wang et al., 2022; Wei et al., 2024). *Pdzklip1*-CreER *R26*$^{Tom/Tom}$ *Kras*^{G12D} mice 3 wk after tamoxifen induction were treated with MRTX1133 twice a day for 1 wk and euthanized (Fig. 8 D). Consistent with the high specificity of MRTX1133 for KRAS^{G12D}, the treatment did not affect the BM cellularity (Fig. 8 E) or the fractions of total (i.e., combined Tom+ and Tom−) stem/progenitor cells within the BM (Fig. 8 F) in *Kras*^{G12D} reporter mice. Furthermore, MRTX1133-treated *Kras*^{G12D} reporter mice showed no reduction of Tom+ Kras-mutant cells in HSC or ST-HSC (Fig. 8 G). In

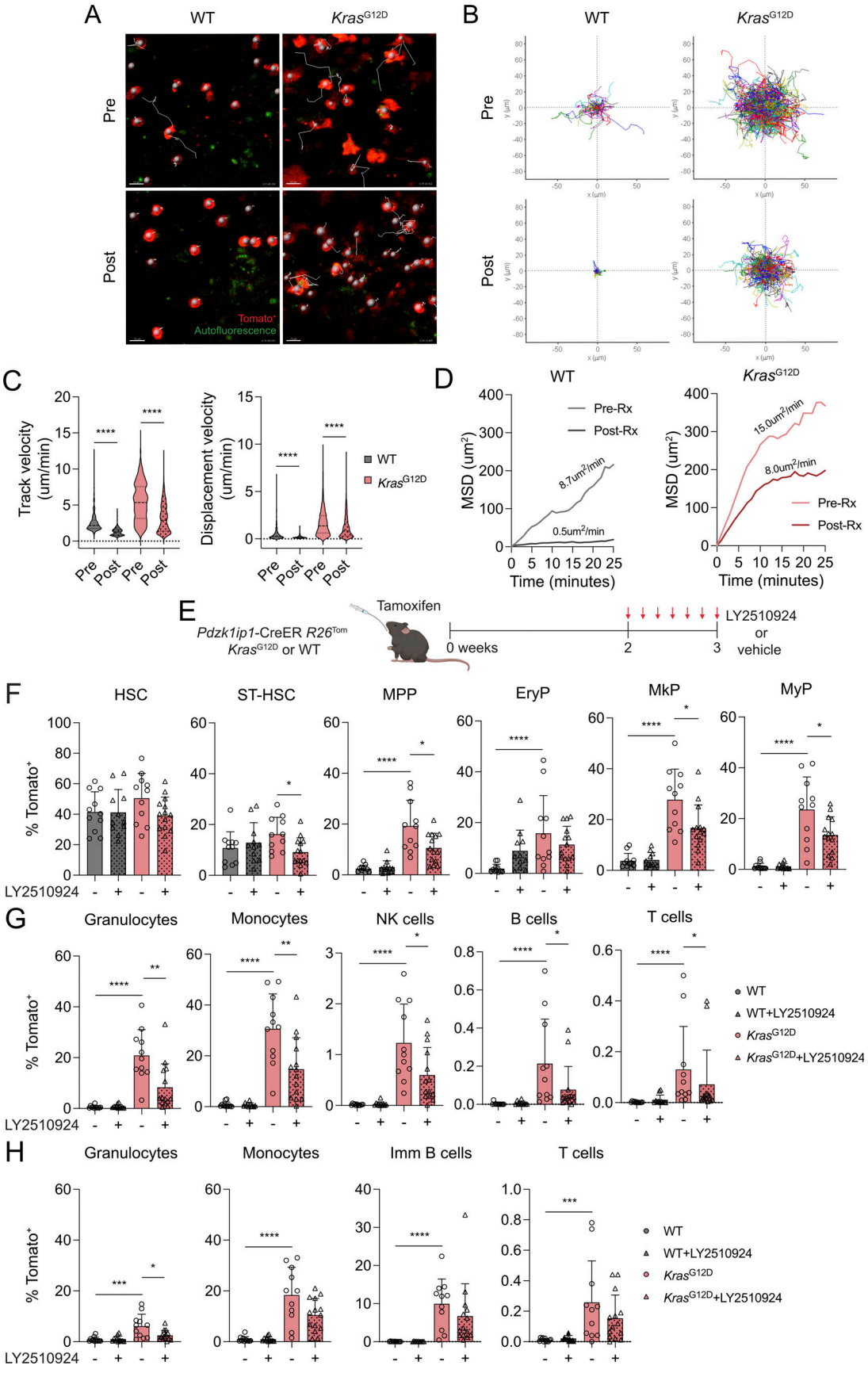

Figure 7. **Blockade of CXCR4-driven motility delays the contribution of *Kras*-mutant HSC. (A)** Representative snapshots of intravital imaging of reporter mice before or after the administration of the CXCR4 inhibitor LY2510924. Red and green signals represent Tom+ cells and autofluorescent macrophages,

respectively; select Tom+ cells are marked by gray spheres, and their tracks are indicated. Data are representative of two to three mice per group. Scale bar, 10 µm. **(B)** Representative flower plots showing tracks of individual Tom+ cells (marked by different colors) relative to each cell's starting point before or after treatment with LY2510924. **(C and D)** Track velocity and displacement velocity of Tom+ cells before and after treatment with LY2510924 (C) and their corresponding MSD (D). Individual Tom+ WT cells (426 cells from three mice) and Tom+ *Kras*-mutant cells (1,108 cells from two mice) were analyzed. Lines on violin plots indicate median and quartiles; on MSD graphs, MSD values are plotted as a function of time and MSD rates for each condition, determined by linear regression analyses, are indicated. **(E)** Effect of CXCR4 antagonist on the contribution of $Kras^{G12D}$-mutant HSC to hematopoiesis. $Kras^{G12D}$ or WT reporter animals were induced with tamoxifen, and 2 wk later were injected s.c. with LY2510924 or PBS twice a day for 1 wk, followed by endpoint analysis. **(F–H)** Accrual of *Kras*-mutant cells in reporter mice after LY2510924 or control treatment. Shown are the fractions of Tom+ cells in the stem/progenitor cells in the BM (F) and mature cells in the spleen (G) and BM (H). Symbols represent individual mice; bars represent the mean ± SD of the data pooled from three independent experiments. Statistical significance was estimated by unpaired Student's *t* test (C) or the Mann–Whitney test (other panels). *P < 0.05, **P < 0.01, ***P < 0.001, ****P < 0.0001.

contrast, Tom+ cells were significantly reduced greater than threefold among MPP and downstream progenitors (Fig. 8 G) and among all mature lineages including T cells (Fig. 8 H). Accordingly, Tom+ cells were virtually eliminated in the thymus of $Kras^{G12D}$ reporter mice (Fig. 8 I). Thus, Kras inhibitors selectively impair the expansion of mutant multipotent and lineage-committed progenitors, although an effect on HSC cannot be completely ruled out.

Finally, we tested the durability of the inhibitor effect by treating the $Kras^{G12D}$ or WT reporter mice between 3 and 4 wk after induction with MRTX1133, and allowing them to recover for 3 wk (Fig. 9 A). We chose MRTX1133 over PD0325901/GDC-0941 given its above-mentioned specificity for $KRAS^{G12D}$, as well as its exclusive effect on mutant MPP but not on HSC (Fig. 8 G). PB tracing showed that MRTX1133 had no effect on the accrual of Tom+ cells in WT reporter mice immediately after the treatment (4 wk) or following the recovery (7 wk) (Fig. 9, B and C). In contrast, MRTX1133 treatment of $Kras^{G12D}$ reporter mice reduced the expanded fraction of Tom+ cells ~2-fold in granulocytes, ~4-fold in monocytes, and ~3-fold in lymphocytes at 4 wk (Fig. 9 B). These data are consistent with the endpoint analysis of MRTX1133-treated $Kras^{G12D}$ reporter mice at 4 wk (Fig. 8 H) and confirm the specificity of MRTX1133 for *Kras*-mutant cells. Following the 3-wk recovery, the reduction of Tom+ cells in MRTX1133-treated $Kras^{G12D}$ reporter mice was no longer significant in granulocytes and diminished to <1.3-fold in monocytes (Fig. 9 C). Accordingly, Tom+ cells were no longer reduced among myeloid cells in the spleen of MRTX1133-treated $Kras^{G12D}$ reporter mice at the postrecovery endpoint (Fig. 9 D). The fraction of Tom+ cells was still reduced ~2-fold in lymphocytes, likely due to the longer lifespans of the latter. Within the stem/progenitor compartment, Tom+ cells were unaffected in HSC, and reduced ~1–5-fold among ST-HSC and MPP and ~1.2-fold among committed progenitors (Fig. 9 E), in contrast to the much stronger reduction immediately after the treatment (Fig. 8 G). Similarly, the massive expansion of Tom+ thymocytes was no longer reduced in MRTX1133-treated mice (Fig. 9 F). The caveats of this experiment include the reduced concordance of $Kras^{G12D}$ induction and Tom expression at 7 wk (Fig. S1 A), and a trend toward higher labeling of HSC in the $Kras^{G12D}$ versus WT reporters (Fig. 8 G and Fig. 9 E), which may mask some effects of MRTX1133 on HSC. Nevertheless, collectively these data suggest that (1) therapeutic inhibition of Kras signaling reduces the early expansion of *Kras*-mutant cells; (2) mutant MPP and downstream progenitors are diminished by the therapy but rebound after its cessation; and (3) mutant HSC are less affected by the therapy than MPP, thus providing a durable reservoir of the mutation.

Discussion

We employed HSC-specific inducible Cre recombination to trace the natural history of leukemia-associated mutations as they progress from HSC to mature lineages in unmanipulated animals. This system revealed that the transforming $Kras^{G12D}$ mutation dramatically accelerated multilineage HSC contribution, equilibrating the labeling of mutant HSC and their progeny within 5–7 wk compared with 1–2 years required for normal HSC (Jang et al., 2023). This was in contrast to the deletion of *Tet2*, which did not affect the net contribution of the HSC population to steady-state hematopoiesis. Importantly, our tracing may have been affected by the incomplete correlation of *Tet2* deletion with reporter expression, and/or missed the expansion of individual clones (Schiroli et al., 2024). On the other hand, our results are consistent with the persistence of *TET2* mutations in healthy humans with ARCH for many years, and with very slow latency or absence of leukemogenesis in *Tet2*-deficient mice, respectively (Ko et al., 2011; Li et al., 2011; Moran-Crusio et al., 2011; Quivoron et al., 2011). Notably, a combination of HSC-specific *Tet2* deletion with inflammatory stimulation resulted in a significant increase in HSC contribution to MyP and mature cells, in agreement with previous reports (Abegunde et al., 2018; Cai et al., 2018; Meisel et al., 2018) and supporting the emerging role of inflammation in ARCH and myeloid malignancy (Avagyan and Zon, 2023; Balandrán et al., 2023; Jakobsen et al., 2024; King et al., 2020). Thus, transforming mutations such as activated Kras appear distinct from ARCH-associated mutations in their major effect on HSC contribution in the steady state.

Unexpectedly, Kras-mutant HSC showed only limited transcriptomic abnormalities and no increased proliferation, unlike the hyperproliferative HSC reported in mice with a constitutive $Kras^{G12D}$ activation (Sabnis et al., 2009). However, HSC in the latter study were defined as $Flt3^-$ LSK cells; this definition would include MPP3, which are shown herein to undergo expansion and hyperproliferation following $Kras^{G12D}$ activation. Indeed, the frequency of functional HSC in this system was reduced, while their contribution to hematopoiesis was increased (Sabnis et al., 2009), consistent with our data. In contrast to HSC, mutant MPP (including both MPP3 and MPP4) showed rapid expansion, increased proliferation, and a distinct transcriptional signature

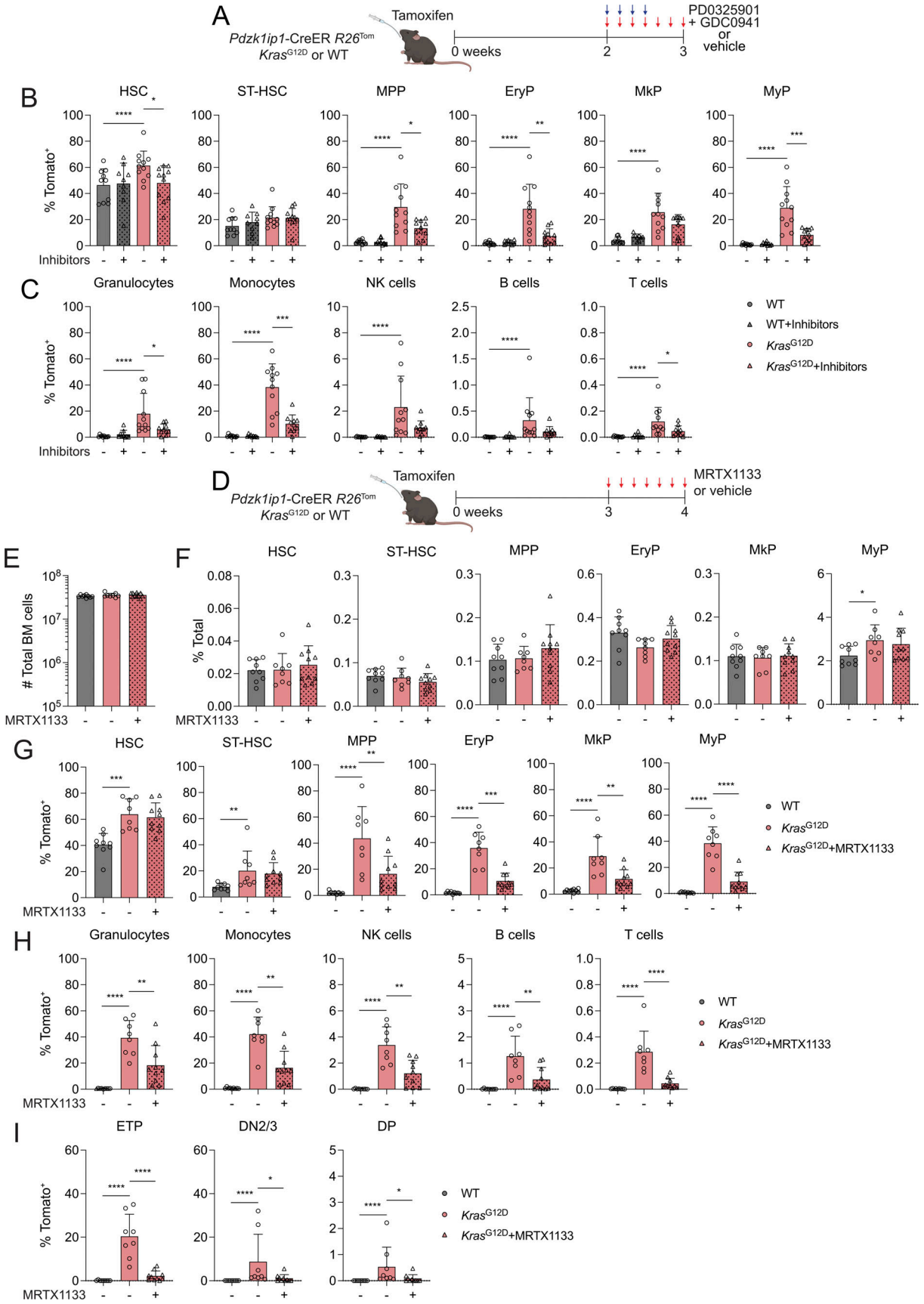

Figure 8. **Kras inhibitors reduce the expansion of Kras-mutant cells. (A)** Effect of combined MEK/ERK/PI(3)K blockade on the contribution of *Kras*^{G12D}-mutant HSC to hematopoiesis. *Kras*^{G12D} or WT reporter animals were induced with tamoxifen, and 2 wk later were treated with mirdametinib (PD0325901) for

4 days (blue arrows) and pictilisib (GDC0941) for 7 days (red arrows) or vehicle, followed by endpoint analysis. **(B and C)** Accrual of *Kras*-mutant cells in reporter mice after the PD0325901+GDC-0941 or control treatment. Shown are the fractions of Tom$^+$ cells in the stem/progenitor cells in the BM (B) and mature cells in the spleen (C). Symbols represent individual mice; bars represent the mean ± SD of the data pooled from two independent experiments. Note that the number of small molecule-treated *Kras*^{G12D} reporter mice is 11 in panel B and 10 in panel C. **(D)** Effect of KRAS^{G12D} inhibitor on the contribution of *Kras*^{G12D}-mutant HSC to hematopoiesis. *Kras*^{G12D} reporter animals were induced with tamoxifen, and 3 wk later were treated with MRTX1133 or vehicle daily for 7 days (red arrows), followed by endpoint analysis. Vehicle-treated WT reporter mice were used as a control to ascertain the effect of Kras. **(E and F)** Absolute number of total BM cells (E) and fractions of stem/progenitor cells among total BM cells (F) in reporter mice after the MRTX1133 or control treatment. **(G–I)** Accrual of *Kras*-mutant cells in reporter mice after the MRTX1133 or control treatment. Shown are the fractions of Tom$^+$ cells in the stem/progenitor cells in the BM (G), mature cells in the spleen (H), and developing T cells in the thymus (I). In panels E–H, symbols represent individual mice; bars represent the mean ± SD of the data pooled from two independent experiments. Statistical significance was estimated by the Mann–Whitney test. *P < 0.05, **P < 0.01, ***P < 0.001, ****P < 0.0001.

characterized by increased differentiation and lymphoid priming. The latter was associated with a particularly rapid contribution of mutant HSC to lymphopoiesis, compared with the slow and stochastic contribution of normal HSC (Upadhaya et al., 2018). This is consistent with the activation of multiple signaling pathways including JAK/STAT, ERK, and mTOR by KRAS^{G12D} in hematopoietic stem/progenitor cells, resulting in hyperproliferation in vitro (Van Meter et al., 2007). An important question raised by these findings is why KRAS activation has a relatively minor effect on HSC but a dramatic effect on MPP. One likely explanation is the glycolysis-driven relative metabolic quiescence of HSC (Kasbekar et al., 2023; Snoeck, 2017), which may "resist" the enhanced signaling induced by KRAS^{G12D}. However, this may not be the sole explanation, because even the more active downstream progenitors were affected less than MPP in terms of their proliferation or transcriptome. One potentially relevant mechanism is Flt3 signaling, which is induced at the HSC-to-MPP transition and is subsequently downregulated in committed progenitors. While Kras activation may be insufficient to fully substitute for the absent Flt3 signaling in HSC, it may synergize with the physiological Flt3 signaling in MPP to enhance their proliferation and lineage priming, as shown in immature lymphocytes (Li et al., 2010). Indeed, both normal and aberrantly activated Flt3 signaling activate Kras (Köthe et al., 2013), and Ras pathway activation accounts for the resistance of myeloid leukemia to FLT3 inhibitors (McMahon et al., 2019). Collectively, these data emphasize the distinction between stem cells as the cells of origin of the mutation, and their progeny as targets of the mutation's activity.

The progeny of Kras-mutant HSC completely took over the MPP compartment within 1 wk, showing a dramatic competitive advantage over their normal counterparts. This is likely facilitated by the observed increase in their proliferation rate; however, the proliferation was accompanied by the correspondingly increased differentiation into downstream lineages, but not by the acquisition of self-renewal capacity. Therefore, additional mechanisms such as the observed upregulation of *Tnf* and *Spp1* may confer an advantage specifically to mutation-carrying MPP. TNF-α (encoded by *Tnf*) and other TNF family members may modulate stroma-derived factors such as IL-7 (Feng et al., 2023); however, given its complex role in HSC biology (Yamashita and Passegué, 2019), its role in Kras-mutant MPP would have to be explored in the future. Here, we found that the global deletion of *Spp1* (encoding osteopontin) delayed the initial expansion of *Kras*^{G12D} MPP, albeit it did not prevent it in the longer term. This was in contrast to the minor impact of osteopontin loss on the HSC-driven hematopoietic flux in the steady state. Osteopontin is a complex glycoprotein that is secreted by stromal cells (particularly osteoblasts) and processed by thrombin, with the resulting fragments binding to CD44 and integrins on stem/progenitor cells and restricting their growth (Cao et al., 2019; Grassinger et al., 2009; Stier et al., 2005). It is possible that Kras activation may facilitate the resistance of mutant MPP to stroma-derived osteopontin. In addition, given that osteopontin was ectopically expressed in Kras-mutant MPP, this expression may facilitate their expansion by inhibiting the proliferation of normal MPP. Of note, thrombin-cleaved osteopontin facilitates lymphopoiesis (Guidi et al., 2017; Kanayama et al., 2017), in agreement with the observed lymphoid priming of mutant MPP. This scenario is also consistent with the elevated levels of osteopontin in myeloid leukemia patients (Liersch et al., 2012) and its cell-intrinsic role in the mouse model of myeloid leukemia (Zhou et al., 2022) and in other Kras-driven tumors such as lung adenocarcinoma (Giopanou et al., 2020; Wang et al., 2017). Even if indirect, our data suggest that mutation-carrying progenitors may utilize a secreted mediator such as osteopontin to outcompete their normal counterparts.

Another mechanism associated with the competitive advantage of Kras-mutant progenitors was their increased motility driven by the chemokine receptor CXCR4. Whereas activated Kras is known to increase the motility of tumor cells (Okudela et al., 2004; Pollock et al., 2005), our data demonstrate the same phenomenon in Kras-mutant progenitor cells prior to overt transformation. Most progenitor cells in the BM are motile in a CXCR4-dependent manner, including HSC (Upadhaya et al., 2020) and B-cell progenitors (Beck et al., 2014). In the latter case, CXCR4-driven motility allowed progenitors to resist the high shear force of the blood flow and hence facilitated their retention in the BM. We found that *Kras*^{G12D}-expressing cells manifested increased motility in their native BM niche before and during their expansion, even though this analysis did not capture specific cell types. This motility was CXCR4-dependent, corresponding to the elevated expression of CXCR4 on mutant MPP. Most importantly, in vivo pharmacological blockade of CXCR4 reduced the motility and delayed the expansion of *Kras*^{G12D} MPP and their contribution to mature lineages. Indeed, motility facilitates a continuous interaction with multiple stromal cells (Upadhaya et al., 2020) and hence the reception of signals derived from them, such as CXCL12 (Greenbaum et al.,

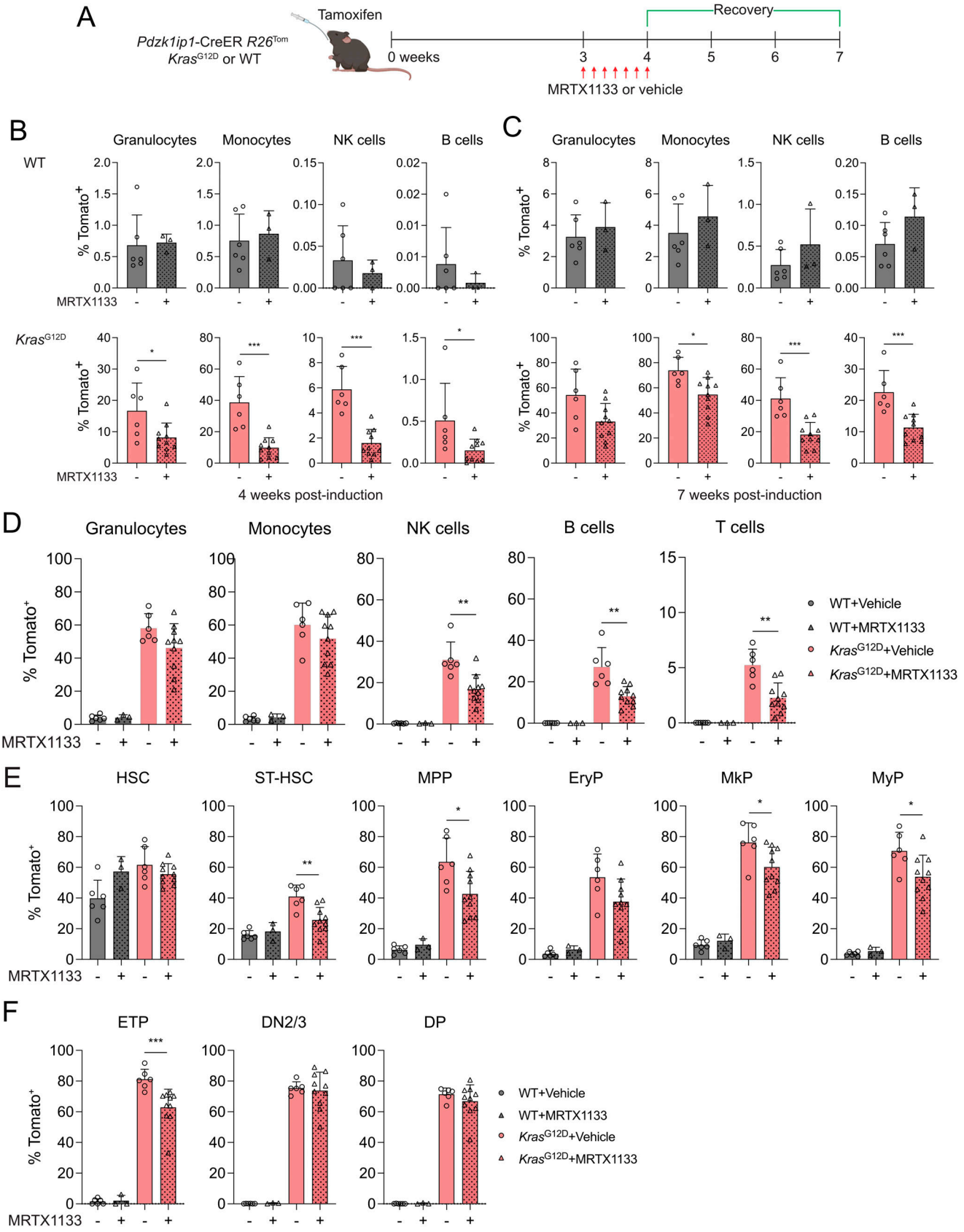

Figure 9. **Expansion of Kras-mutant cells resumes after the cessation of the therapy. (A)** Contribution of *Kras*^{G12D}-mutant HSC to hematopoiesis after the treatment with KRAS^{G12D} inhibitor followed by recovery. *Kras*^{G12D} or WT reporter animals 3 wk after tamoxifen administration were treated with MRTX1133 or vehicle daily for 7 days (red arrows), followed by 3 wk of recovery and endpoint analysis. **(B and C)** Accrual of Tom$^+$ cells in the blood after the treatment (week

4, B) or recovery (week 7, C). Shown are fractions of Tom+ cells within the indicated blood cell types in MRTX1133- or vehicle-treated WT (gray, top panels) or *Kras*^{G12D} (red, bottom panels) reporter mice. Note the different scales for WT and *Kras*^{G12D} mice, reflecting the expansion of Tom+ cells in the latter. **(D–F)** Accrual of *Kras*-mutant cells in reporter mice after the recovery from MRTX1133 treatment. Shown are the fractions of Tom+ cells in the mature cells in the spleen (D), stem/progenitor cells in the BM (E), and developing T cells in the thymus (F). In panels B–F, symbols represent individual mice; bars represent the mean ± SD of the data pooled from two independent experiments. Statistical significance was estimated by the Mann–Whitney test. *P < 0.05, **P < 0.01, ***P < 0.001.

2013) and membrane-bound Kit ligand (Ding et al., 2012). In addition, hyperactive CXCR4 may alter the BM stromal compartment (Zehentmeier et al., 2022), which may further impair the function of normal stem/progenitor cells. Because CXCR4-dependent motility and maintenance appear linked, these results suggest that mutation-carrying progenitors may outcompete normal cells by "outrunning" them in their BM niche. However, a motility-independent role of CXCR4 in the maintenance and expansion of Kras-mutant progenitors is entirely possible. CXCR4 represents a promising therapeutic target in leukemia (Cancilla et al., 2020) and in particular is important for the propagation of T-ALL in their BM niche (Hawkins et al., 2016; Passaro et al., 2015; Pitt et al., 2015). Our data suggest that it may also be important for the initial spread of mutant cells in the preleukemic state.

Collectively, our system reveals a striking effect of a common transforming mutation on the normal HSC-driven hematopoiesis long before the onset of leukemia. Surprisingly, this mutation did not affect HSC behavior but reprogrammed MPP into hypercompetitive cells that hijack normal hematopoiesis. In this "two-component" model, HSC serve as a source and long-term reservoir of the mutation, whereas the reprogrammed progenitors rapidly spread the mutation into all lineages. This model is consistent with the reconstructions of single-cell trajectories in human leukemia, which suggest that mutations arise in stem cells and are selected at the level of progenitors (Beneyto-Calabuig et al., 2023; Nam et al., 2022; Van Egeren et al., 2021). Moreover, it underscores the ability of current mutation-targeting therapies to expunge mutant progenitors and their progeny, but not the upstream reservoir of the mutation (Pollyea and Jordan, 2017; Schepers et al., 2015). The latter likely serves as a basis for subsequent disease relapses and should represent the key target of next-generation therapies for hematological malignancies.

Materials and methods

The antibodies, animal strains, reagents, software, and genotyping primers are listed in Table S3.

Animals

All animal studies were performed according to the investigator's protocol approved by the Institutional Animal Care and Use Committee of New York University Grossman School of Medicine (NYUGSoM). *Pdzklip1*-CreER transgenic mouse strain was crossed with the Cre-inducible *R26*^{Tom} reporter strain on C57BL/6 genetic background as described previously (Sawai et al., 2016; Upadhaya et al., 2018). All *R26*^{Tom} mice were homozygous for the reporter allele. Mice of either sex were used, as no major differences in the efficiency or specificity of labeling were observed between them. *Pdzklip1*-CreER *R26*$^{Tom/Tom}$ reporter animals were crossed with *Tet2*^{flox} mice ([Moran-Crusio et al., 2011] maintained by the Aifantis Lab at NYUGSoM). *Pdzklip1*-CreER *R26*$^{Tom/Tom}$ mice were also crossed with LSL-*Kras*^{G12D} mice (Jackson et al., 2001) on pure C57BL/6 background (strain 008179; Jackson Laboratories) to generate reporter mice heterozygous for the *Kras*^{G12D} allele. In addition, *Pdzklip1*-CreER *R26*$^{Tom/+}$ *Kras*^{G12D} mice were crossed with *Spp1*$^{-/-}$ mice (Liaw et al., 1998) on pure C57BL/6 background (strain 004936; Jackson Laboratories).

Animal procedures

To induce Cre recombination, mice were administered with the different concentrations of tamoxifen (Sigma-Aldrich) in sunflower oil by gavage: 0.5 mg (*Kras*^{G12D} and control reporter mice) or 1 mg (*Tet2*$^{fl/fl}$ and control reporter mice). PB sampling and BM biopsy were conducted as described previously (Sawai et al., 2016). Briefly, blood (~100 µl) was collected by submandibular vein puncture with a sterile disposable lancet. BM biopsy was performed on isoflurane-anesthetized mice by inserting a 28.5G insulin syringe needle into the joint surface of the femur through the patellar tendon and then into the bone cavity. Up to 20 µl of the BM suspension (~10^6 cells) was harvested. At the endpoint, animals were sacrificed and single-cell suspensions were prepared from the BM (femora and tibiae), spleens, and thymi, counted, and analyzed by flow cytometry.

To mimic microbial stimulation, *Pdzklip1*-CreER *R26*$^{Tom/Tom}$ *Tet2*$^{fl/fl}$ mice were injected i.p. with 0.1 mg of the TLR2 agonist Pam3CSK4 for 3 consecutive days starting from the day of tamoxifen treatment. To block CXCR4 in vivo, *Pdzklip1*-CreER *R26*$^{Tom/Tom}$ or *Pdzklip1*-CreER *R26*$^{Tom/Tom}$ *Kras*^{G12D} reporter mice were induced with tamoxifen, and 2 wk later were injected s.c. with LY2510924 (3 mg/kg) or PBS twice a day for 7 days, followed by euthanasia.

For small molecule treatments, *Pdzklip1*-CreER *R26*$^{Tom/Tom}$ *Kras*^{G12D} or WT mice were induced with tamoxifen, and 2 wk later were treated concomitantly with GDC-0941 (100 mg/kg) daily for 7 days and with PD0325901 (5 mg/kg) for the first 4 days via oral gavage, followed by euthanasia. The chemicals were dissolved in 0.5% carboxymethylcellulose sodium (CMC-Na). Control mice were treated in a similar way with the vehicle (CMC-Na) only. To directly inhibit the mutant KRAS^{G12D} protein, *Pdzklip1*-CreER *R26*$^{Tom/Tom}$ *Kras*^{G12D} or WT mice were induced with tamoxifen, and after 3 wk were administered with MRTX1133 (30 mg/kg) via i.p. injection twice a day for 7 days, and euthanized since the last injection or 3 wk later for the endpoint analysis. MRTX1133 was dissolved in 10% sulfobutylether-β-cyclodextrin (SBE-β-CD) in 50 mM citrate buffer, pH

5.0. Control mice were treated in a similar way with the vehicle (10% SBE-β-CD) only.

To test the reconstitution capacity of Kras-mutant progenitors, *Pdzklip1*-CreER *R26*$^{Tom/Tom}$ *Kras*^{G12D} mice were administered with tamoxifen and euthanized 5 wk later. Sorted Tom$^+$ HSC (50 cells) or Tom$^+$ MPP (1,000 cells) were mixed with 2 × 10^5 total BM cells from CD45.1 congenic mice and transferred into lethally irradiated CD45.1 congenic recipients. Two donor mice were induced, and donor cells from each mouse were transferred separately. PB was collected, stained with flow antibodies, and analyzed with the fractions of donor-derived Tom$^+$ cells in the mature blood cell types up to 3 mo after transplantation.

Cell staining and flow cytometry

Cells from PB, BM, spleens, and thymi were suspended in 2% FBS-contained PBS after red blood cell lysis and wash. Cells were stained with indicated fluorochrome-conjugated antibodies (Table S3) for 20 or 60 min in 2% FBS-containing PBS. Samples were acquired on an Attune NxT flow cytometer (Thermo Fisher Scientific) and analyzed using FlowJo software (FlowJo, LLC). The definition of cell populations is described below.

For stem/progenitor staining, the lineage cocktail included antibodies of CD11b, CD11c, B220, TCRβ, Gr-1, NKp46, and Ter119, HSC (LSK CD150$^+$ CD48$^-$), ST-HSC (LSK CD150$^-$ CD48$^-$), MPP (LSK CD150$^-$ CD48$^+$), EryP (Lin$^-$ Sca-1$^-$ c-Kit$^+$ CD150$^+$ CD41$^-$), MkP (Lin$^-$ Sca-1$^-$ c-Kit$^+$ CD150$^+$ CD41$^+$), MyP (Lin$^-$ Sca-1$^-$ c-Kit$^+$ CD150$^-$ CD41$^-$), common myeloid progenitors (Lin$^-$ Sca-1$^-$ c-Kit$^+$ CD16/32$^-$ CD34$^+$), granulocyte–monocyte progenitors (Lin$^-$ Sca-1$^-$ c-Kit$^+$ CD16/32$^+$ CD34$^+$), and MEP (Lin$^-$ Sca-1$^-$ c-Kit$^+$ CD16/32$^-$ CD34$^-$). The expression of IL-7Ra was measured in Sca-1$^-$ c-Kit$^-$ and c-Kit$^{lo/int}$ progenitors, Sca-1$^-$ c-Kit$^+$ MyP, and Sca-1$^+$ c-Kit$^+$ MPP4. Subsets of B cells in the BM were identified as pre-pro B (IgD$^-$ IgM$^-$ B220$^+$ CD43$^+$ CD93$^+$ CD19$^-$), pro B (IgD$^-$ IgM$^-$ B220$^+$ CD43$^+$ CD93$^+$ CD19$^+$), pre B (IgD$^-$ IgM$^-$ B220$^+$ CD43$^-$ CD93$^+$ CD19$^+$), and Imm B (IgD$^-$ IgM$^+$ B220$^+$ CD43$^-$ CD93$^+$ CD19$^-$). Thymocytes were determined as ETP (CD4$^-$ CD8$^-$ Lin$^-$ CD44$^+$ CD25$^-$ c-Kit$^+$), double-negative thymocytes 2/3 (DN2, CD4$^-$ CD8$^-$ Lin$^-$ CD25$^+$), double-negative thymocytes 4 (DN4, CD4$^-$ CD8$^-$ CD44$^-$ CD25$^-$), DP thymocytes (CD4$^+$ CD8$^+$ TCRβ$^-$), CD4 T cells (CD4$^+$ CD8$^-$ TCRβ$^+$), and CD8 T cells (CD4$^-$ CD8$^+$ TCRβ$^+$). Immune cells in PB, BM, and spleen were defined as platelets (Plt, low forward and side scatter, Ter119$^-$ CD150$^+$ CD41$^+$), granulocytes (Neu, TCRβ$^-$ B220$^-$ NKp46$^-$ CD11b$^+$ Ly6C^{int} Ly6G$^+$), monocytes (Mono, TCRβ$^-$ B220$^-$ NKp46$^-$ CD11b$^+$ Ly6C^{hi}), NK cells (NK, TCRβ$^-$ B220$^-$ NKp46$^+$), B cells (B, CD11b$^-$ Ly6C$^-$ Ly6G$^-$ NKp46$^-$ B220$^+$), and T cells (T, CD11b$^-$ Ly6C$^-$ Ly6G$^-$ NKp46$^-$ TCRβ$^+$).

EdU cell proliferation assay

Pdzklip1-CreER *R26*^{Tom} *Kras*^{G12D} or WT mice were administered 0.5 mg of tamoxifen. 3 or 5 wk later, they were injected with 1 mg of EdU i.p. and euthanized 2 h later. EdU incorporation was measured by flow cytometry using Click-iT Plus EdU Alexa Fluor 488 Flow Cytometry Assay Kit. In some experiments, mice induced with tamoxifen 3 wk earlier were injected with 1 mg EdU on two consecutive days and euthanized 48 h after the first injection. Cells were stained for EdU incorporation as above, along with DNA content using FxCycle Violet Stain.

CITE-seq sample preparation

Pdzklip1-CreER *R26*^{Tom} or *Pdzklip1*-CreER *R26*^{Tom} *Kras*^{G12D} mice were treated with 0.5 mg of tamoxifen. After 3 wk after induction, mice were sacrificed and femora, tibiae, humerus, and pelvises were isolated. Bones were flushed with 2% FBS-contained PBS, and red blood cell lysis was performed. Lineage cells were depleted with a magnetic enrichment step (Streptavidin MicroBeads; Miltenyi) using a cocktail biotinylated antibodies against B220, TCRβ, NKp46, Ter119, CD11b, and Gr-1. After lineage depletion, the resulting cells were stained with TruStain FcX Fc Blocking Reagent (BioLegend) followed by incubation with PB-conjugated lineage antibodies, c-Kit, Sca-1, and live/dead cell dye, as well as TotalSeq B hashtags (BioLegend). For the *Kras*^{G12D} group, ∼10,000 Tom$^+$ LSK cells were sorted per mouse, and for the WT group, ∼10,000 total LSK cells were sorted per mouse. Cells from two individual mice per group (four hashtagged samples) or four different hashtag-connected samples were pooled, and the resulting cell mixture was prepared according to the 10x Genomics protocol and loaded onto the 10x Chromium Controller for gel beads-in-emulsion generation and barcoding. Libraries were prepared and sequenced using Illumina NovaSeq 6000 at the Genome Technology Core at NYUGSoM.

CITE-seq analysis

Reads from fastq files were processed using 10X Genomics' *Cellranger count* pipeline (v.6.0.1). Demultiplexing of hashtags was performed using Seurat's *HTODemux* method, with resulting singlets passed into iCellR for quality control (QC) and dimensionality reduction using *KNetL* with zoom setting set to 500 and sensitivity set to 500—resulting in nine clusters. QC settings included the following: mitochondrial reads for a given cell <5% of reads while retaining only those cells with between 200 and 6,000 genes, yielding 11,781 cells. One cluster was identified as a contaminant and removed, yielding 10,594 cells. For the pairwise comparison of selected populations, the *iCellR* (*v.1.6.7*) cluster-wise (cell type), condition-wise (WT, KRAS) comparisons were performed using the *run.diff.exp* method with "*clustBase.condComp*" argument. For each cell type and each gene independently, cells were grouped by condition with the Wilcoxon rank-sum test performed on the means of the two groups.

Intravital imaging

Pdzklip1-CreER *R26*$^{Tom/Tom}$ or *Pdzklip1*-CreER *R26*$^{Tom/Tom}$ *Kras*^{G12D} mice were treated with 0.5 mg tamoxifen. 2 or 3 wk later, mice were examined by intravital two-photon laser scanning microscopy of the tibial BM as described previously (Upadhaya et al., 2020). Mice were anesthetized with isoflurane inhalation and secured in a supine position to an imaging plate heated to 37°C. An incision was made in the lower leg, and soft tissue was removed to expose the medial region of the tibia. The medial tibia was thinned to a thickness of ∼200 µm using a microdrill. A custom-built appliance with an opening was used to immobilize the leg and to expose the drilled bone to the microscope

objective. A water-tight immersion well lined with vacuum grease was made on the appliance over the exposed bone and filled with warm lactated Ringer's solution for the microscope objective. Mice were anesthetized with isoflurane inhalation during the entire intravital imaging session. To block CXCR4 in vivo, mice were imaged for 60 min as above, injected i.v. with 3 mg/kg of LY2510924 in PBS, and imaged for a further 60 min.

Two-photon images were acquired with an Olympus FV1000-MPE upright laser scanning microscope equipped with a 25× 1.05NA water immersion objective and Mai Tai DeepSee Ti:Sapphire pulsed laser (Spectra-Physics) that was tuned to 920 nm. The microscope was fitted with a custom-built incubated chamber to maintain a temperature of 37°C and block infiltrating room light. Movies were recorded for ∼60 min, and frames were acquired continuously without breaks. Each frame consisted of a 512 × 512 µm Z-stacked image that was 75–90 µm deep and acquired in 3-µm-thick slices. The amount of time elapsed between each consecutive frame was 45–55 s, depending on the depth of imaging.

Intravital imaging analysis

Image analysis was conducted using Imaris software 9.3. Cells were detected based on size and fluorescence and tracked three-dimensionally in autoregressive motion mode. Red tdTomato fluorescence was distinguished from background autofluorescence and channel bleed-through by creating ratio and subtracted channels. Drift correction was performed by three-dimensionally tracking sessile autofluorescent macrophages and correcting XYZ registrations over time. Track velocity was measured as the sum of the displacements between all consecutive time point pairs of a given cell track (e.g., t1 and t2, t2 and t3) divided by the total real-time duration of the track in minutes. Displacement velocity was measured as the distance between the first and last positions of a given cell track divided by the total real-time duration of the track in minutes. MSD is a composite measurement of all cell tracks in a given movie. For each time point of a movie converted to real-time minutes, the square of the distance between a cell's initial position and the cell's current position was averaged for all present cell tracks. For accuracy, only the linear portions of the MSD functions were analyzed.

Migration assay

Pdzklip1-CreER *R26*^{Tom} or *Pdzklip1*-CreER *R26*^{Tom} *Kras*^{G12D} mice were treated with 0.5 mg of tamoxifen. 3 wk later, mice were euthanized and lineage-negative cells were isolated by magnetic negative selection as described above for CITE-seq, but with additional antibodies to CD11c, CD115, CD16/32, and CD41 to deplete committed progenitors.

The migratory capacity was assayed using 6.5-mm transwells with 5.0 µm pore polycarbonate membrane (Corning). Cells were resuspended in RPMI medium supplemented with 0.5% BSA, penicillin/streptomycin, L-glutamine, and 50 µM 2-mercaptoethanol at 3 × 10^4 cells/100 µl and incubated for 2 h at 37°C. Medium containing CXCL12 (100 ng/ml in 600 µl) was added to the bottom wells; cells were added to the upper chamber and incubated for 4 h at 37°C. Cells migrated to the bottom wells were harvested, and the numbers of Tom$^+$ or Tom$^-$ cells were determined by flow cytometry. Migration was measured as a percentage of migrated cells out of the total input for Tom$^+$ or Tom$^-$ cells.

Detection of recombined *Tet2*$^{fl/fl}$ or *Kras*^{G12D} allele

For *Pdzklip1*-CreER *R26*$^{Tom/Tom}$ *Tet2*$^{fl/fl}$ mice, Tom$^+$ versus Tom$^-$ LSK cells were sorted at 3 wk after tamoxifen treatment, or Tom$^+$ versus Tom$^-$ total BM cells were sorted at 6 mo after tamoxifen treatment. Genomic DNA was extracted by using Quick-DNA Miniprep Kit, and the recombination of *Tet2*$^{fl/fl}$ was tested by genomic PCR for the expected amplicon sizes: recombined (null) allele ∼550 bp, floxed allele ∼430 bp, and WT allele ∼250 bp. For *Pdzklip1*-CreER *R26*$^{Tom/Tom}$ *Kras*^{G12D} mice, Tom$^+$ versus Tom$^-$ LSK cells were sorted at 3 wk after tamoxifen treatment, or Tom$^+$ versus Tom$^-$ total BM cells were sorted at 5 or 7 wk after tamoxifen treatment. Genomic PCR was performed for the expected amplicon sizes: recombined (*Kras*^{G12D}) allele ∼650 bp, LSL-cassette allele 500 bp, and WT allele 622 bp. Densitometric analysis of the gels was done in ImageJ2, by determining the density of a fixed area corresponding to each band, and subtracting the background density from the same lane.

Statistical analysis

Statistical significance was determined with the indicated tests using the Prism software (GraphPad).

Online supplemental material

Fig. S1 shows aberrant thymocyte development and T-cell lymphomas in mice with induced *Kras*^{G12D} mutation in HSC. Fig. S2 shows the contribution of *Tet2*-deficient HSC to hematopoiesis in the steady state. Fig. S3 shows increased contribution of *Tet2*-deficient HSC to myelopoiesis after inflammatory stimulation. Fig. S4 shows additional analyses of the CITE-seq data. Fig. S5 shows additional characterization of HSC contribution in osteopontin-deficient mice. Video 1 shows intravital microscopy of Tom$^+$ stem/progenitor cells in WT or *Kras*^{G12D} reporter mice at 2 wk after tamoxifen induction. Video 2 shows intravital microscopy of Tom$^+$ stem/progenitor cells in WT or *Kras*^{G12D} reporter mice at 3 wk after tamoxifen induction. Video 3 shows intravital microscopy of Tom$^+$ stem/progenitor cells in LY2510924-treated WT reporter mice at 3 wk after tamoxifen induction. Video 4 shows intravital microscopy of Tom$^+$ stem/progenitor cells in LY2510924-treated *Kras*^{G12D} reporter mice at 3 wk after tamoxifen induction. Table S1 lists DEG in CITE-seq cell clusters. Table S2 lists DEG between WT and Kras-mutant cells. Table S3 lists antibodies and reagents used in the study. Source data for Fig. 1 B, Fig. S1 A, and Fig. S2 G show uncropped gel images for the respective figures.

Data availability

The CITE-seq data underlying Fig. 4 are openly available in the National Center for Biotechnology Information Gene Expression Omnibus database with the accession number GSE261879. All data in this study are available in the published article and its supplemental materials.

Acknowledgments

We thank Makiko Hayashi and Thales Papagiannakopoulos for advice and help with MRTX1133 treatment. We acknowledge the use of NYU Genome Technology Center, which is partially supported by the Laura and Isaac Perlmutter Cancer Center.

This study was supported by the National Institutes of Health grant HL152637 (to B. Reizis, D.R. Fooksman), the Edward P. Evans Foundation (to B. Reizis), the Hirsch Foundation (to D.R. Fooksman), and SIRIC BRIO (to C.M. Sawai). Trainee support to R. Park was provided by the Medical Scientist Training Program's National Institutes of Health training grant T32 GM149364.

Author contributions: G. Jang: conceptualization, data curation, formal analysis, investigation, methodology, project administration, validation, visualization, and writing—original draft. R. Park: formal analysis, investigation, visualization, and writing—original draft, review, and editing. E. Esteva: data curation, formal analysis, software, visualization, and writing—original draft. P.-F. Hsu: investigation. J. Feng: investigation. S. Upadhaya: writing—review and editing. C.M. Sawai: conceptualization, methodology, and writing—review and editing. I. Aifantis: resources and writing—review and editing. D.R. Fooksman: conceptualization, formal analysis, investigation, methodology, resources, software, supervision, validation, and writing—review and editing. B. Reizis: conceptualization, funding acquisition, project administration, supervision, and writing—original draft, review, and editing.

Disclosures: The authors declare no competing interests exist.

Submitted: 2 April 2024
Revised: 9 November 2024
Accepted: 14 February 2025

References

Abegunde, S.O., R. Buckstein, R.A. Wells, and M.J. Rauh. 2018. An inflammatory environment containing TNFα favors Tet2-mutant clonal hematopoiesis. *Exp. Hematol.* 59:60–65. https://doi.org/10.1016/j.exphem.2017.11.002

Ahmad, H., N. Jahn, and S. Jaiswal. 2023. Clonal hematopoiesis and its impact on human Health. *Annu. Rev. Med.* 74:249–260. https://doi.org/10.1146/annurev-med-042921-112347

Akinduro, O., T.S. Weber, H. Ang, M.L.R. Haltalli, N. Ruivo, D. Duarte, N.M. Rashidi, E.D. Hawkins, K.R. Duffy, and C. Lo Celso. 2018. Proliferation dynamics of acute myeloid leukaemia and haematopoietic progenitors competing for bone marrow space. *Nat. Commun.* 9:519. https://doi.org/10.1038/s41467-017-02376-5

Amann-Zalcenstein, D., L. Tian, J. Schreuder, S. Tomei, D.S. Lin, K.A. Fairfax, J.E. Bolden, M.D. McKenzie, A. Jarratt, A. Hilton, et al. 2020. A new lymphoid-primed progenitor marked by Dach1 downregulation identified with single cell multi-omics. *Nat. Immunol.* 21:1574–1584. https://doi.org/10.1038/s41590-020-0799-x

Avagyan, S., and L.I. Zon. 2023. Clonal hematopoiesis and inflammation - the perpetual cycle. *Trends Cell Biol.* 33:695–707. https://doi.org/10.1016/j.tcb.2022.12.001

Balandrán, J.C., A. Lasry, and I. Aifantis. 2023. The role of inflammation in the initiation and progression of myeloid neoplasms. *Blood Cancer Discov.* 4:254–266. https://doi.org/10.1158/2643-3230.BCD-22-0176

Beck, T.C., A.C. Gomes, J.G. Cyster, and J.P. Pereira. 2014. CXCR4 and a cell-extrinsic mechanism control immature B lymphocyte egress from bone marrow. *J. Exp. Med.* 211:2567–2581. https://doi.org/10.1084/jem.20140457

Beneyto-Calabuig, S., A.K. Merbach, J.A. Kniffka, M. Antes, C. Szu-Tu, C. Rohde, A. Waclawiczek, P. Stelmach, S. Gräßle, P. Pervan, et al. 2023. Clonally resolved single-cell multi-omics identifies routes of cellular differentiation in acute myeloid leukemia. *Cell Stem Cell.* 30:706–721.e8. https://doi.org/10.1016/j.stem.2023.04.001

Braun, B.S., D.A. Tuveson, N. Kong, D.T. Le, S.C. Kogan, J. Rozmus, M.M. Le Beau, T.E. Jacks, and K.M. Shannon. 2004. Somatic activation of oncogenic Kras in hematopoietic cells initiates a rapidly fatal myeloproliferative disorder. *Proc. Natl. Acad. Sci. USA.* 101:597–602. https://doi.org/10.1073/pnas.0307203101

Busch, K., K. Klapproth, M. Barile, M. Flossdorf, T. Holland-Letz, S.M. Schlenner, M. Reth, T. Höfer, and H.R. Rodewald. 2015. Fundamental properties of unperturbed haematopoiesis from stem cells in vivo. *Nature.* 518:542–546. https://doi.org/10.1038/nature14242

Cai, Z., J.J. Kotzin, B. Ramdas, S. Chen, S. Nelanuthala, L.R. Palam, R. Pandey, R.S. Mali, Y. Liu, M.R. Kelley, et al. 2018. Inhibition of inflammatory signaling in Tet2 mutant preleukemic cells mitigates stress-induced abnormalities and clonal hematopoiesis. *Cell Stem Cell.* 23:833–849.e5. https://doi.org/10.1016/j.stem.2018.10.013

Cancilla, D., M.P. Rettig, and J.F. DiPersio. 2020. Targeting CXCR4 in AML and ALL. *Front. Oncol.* 10:1672. https://doi.org/10.3389/fonc.2020.01672

Cao, H., B. Cao, C.K. Heazlewood, M. Domingues, X. Sun, E. Debele, N.E. McGregor, N.A. Sims, S.Y. Heazlewood, and S.K. Nilsson. 2019. Osteopontin is an important regulative component of the fetal bone marrow hematopoietic stem cell niche. *Cells.* 8:985. https://doi.org/10.3390/cells8090985

Chan, I.T., J.L. Kutok, I.R. Williams, S. Cohen, L. Kelly, H. Shigematsu, L. Johnson, K. Akashi, D.A. Tuveson, T. Jacks, and D.G. Gilliland. 2004. Conditional expression of oncogenic K-ras from its endogenous promoter induces a myeloproliferative disease. *J. Clin. Invest.* 113:528–538. https://doi.org/10.1172/JCI20476

Chapple, R.H., Y.J. Tseng, T. Hu, A. Kitano, M. Takeichi, K.A. Hoegenauer, and D. Nakada. 2018. Lineage tracing of murine adult hematopoietic stem cells reveals active contribution to steady-state hematopoiesis. *Blood Adv.* 2:1220–1228. https://doi.org/10.1182/bloodadvances.2018016295

Collins, A., C.A. Mitchell, and E. Passegue. 2021. Inflammatory signaling regulates hematopoietic stem and progenitor cell development and homeostasis. *J. Exp. Med.* 218:e20201545. https://doi.org/10.1084/jem.20201545

Dail, M., Q. Li, A. McDaniel, J. Wong, K. Akagi, B. Huang, H.C. Kang, S.C. Kogan, K. Shokat, L. Wolff, et al. 2010. Mutant Ikzf1, KrasG12D, and Notch1 cooperate in T lineage leukemogenesis and modulate responses to targeted agents. *Proc. Natl. Acad. Sci. USA.* 107:5106–5111. https://doi.org/10.1073/pnas.1001064107

Dail, M., J. Wong, J. Lawrence, D. O'Connor, J. Nakitandwe, S.C. Chen, J. Xu, L.B. Lee, K. Akagi, Q. Li, et al. 2014. Loss of oncogenic Notch1 with resistance to a PI3K inhibitor in T-cell leukaemia. *Nature.* 513:512–516. https://doi.org/10.1038/nature13495

Ding, L., T.L. Saunders, G. Enikolopov, and S.J. Morrison. 2012. Endothelial and perivascular cells maintain haematopoietic stem cells. *Nature.* 481:457–462. https://doi.org/10.1038/nature10783

Eaves, C.J. 2015. Hematopoietic stem cells: Concepts, definitions, and the new reality. *Blood.* 125:2605–2613. https://doi.org/10.1182/blood-2014-12-570200

Fanti, A.K., K. Busch, A. Greco, X. Wang, B. Cirovic, F. Shang, T. Nizharadze, L. Frank, M. Barile, T.B. Feyerabend, et al. 2023. Flt3- and Tie2-Cre tracing identifies regeneration in sepsis from multipotent progenitors but not hematopoietic stem cells. *Cell Stem Cell.* 30:207–218.e7. https://doi.org/10.1016/j.stem.2022.12.014

Feng, J., J.N. Pucella, G. Jang, M. Alcántara-Hernández, S. Upadhaya, N.M. Adams, A. Khodadadi-Jamayran, C.M. Lau, M. Stoeckius, S. Hao, et al. 2022. Clonal lineage tracing reveals shared origin of conventional and plasmacytoid dendritic cells. *Immunity.* 55:405–422.e11. https://doi.org/10.1016/j.immuni.2022.01.016

Feng, X., R. Sun, M. Lee, X. Chen, S. Guo, H. Geng, M. Muschen, J. Choi, and J.P. Pereira. 2023. Cell circuits between leukemic cells and mesenchymal stem cells block lymphopoiesis by activating lymphotoxin beta receptor signaling. *Elife.* 12:e83533. https://doi.org/10.7554/eLife.83533

Fooksman, D.R., T.A. Schwickert, G.D. Victora, M.L. Dustin, M.C. Nussenzweig, and D. Skokos. 2010. Development and migration of plasma cells in the mouse lymph node. *Immunity.* 33:118–127. https://doi.org/10.1016/j.immuni.2010.06.015

Giopanou, I., N.I. Kanellakis, A.D. Giannou, I. Lilis, A. Marazioti, M. Spella, V. Papaleonidopoulos, D.C.M. Simoes, D.E. Zazara, T. Agalioti, et al. 2020.

Osteopontin drives KRAS-mutant lung adenocarcinoma. *Carcinogenesis*. 41:1134–1144. https://doi.org/10.1093/carcin/bgz190

Grassinger, J., D.N. Haylock, M.J. Storan, G.O. Haines, B. Williams, G.A. Whitty, A.R. Vinson, C.L. Be, S. Li, E.S. Sørensen, et al. 2009. Thrombin-cleaved osteopontin regulates hemopoietic stem and progenitor cell functions through interactions with alpha9beta1 and alpha4beta1 integrins. *Blood*. 114:49–59. https://doi.org/10.1182/blood-2009-01-197988

Greenbaum, A., Y.M. Hsu, R.B. Day, L.G. Schuettpelz, M.J. Christopher, J.N. Borgerding, T. Nagasawa, and D.C. Link. 2013. CXCL12 in early mesenchymal progenitors is required for haematopoietic stem-cell maintenance. *Nature*. 495:227–230. https://doi.org/10.1038/nature11926

Guidi, N., M. Sacma, L. Ständker, K. Soller, G. Marka, K. Eiwen, J.M. Weiss, F. Kirchhoff, T. Weil, J.A. Cancelas, et al. 2017. Osteopontin attenuates aging-associated phenotypes of hematopoietic stem cells. *EMBO J*. 36: 840–853. https://doi.org/10.15252/embj.201694969

Hawkins, E.D., D. Duarte, O. Akinduro, R.A. Khorshed, D. Passaro, M. Nowicka, L. Straszkowski, M.K. Scott, S. Rothery, N. Ruivo, et al. 2016. T-cell acute leukaemia exhibits dynamic interactions with bone marrow microenvironments. *Nature*. 538:518–522. https://doi.org/10.1038/nature19801

Jackson, E.L., N. Willis, K. Mercer, R.T. Bronson, D. Crowley, R. Montoya, T. Jacks, and D.A. Tuveson. 2001. Analysis of lung tumor initiation and progression using conditional expression of oncogenic K-ras. *Genes Dev*. 15:3243–3248. https://doi.org/10.1101/gad.943001

Jakobsen, N.A., S. Turkalj, A.G.X. Zeng, B. Stoilova, M. Metzner, S. Rahmig, M.S. Nagree, S. Shah, R. Moore, B. Usukhbayar, et al. 2024. Selective advantage of mutant stem cells in human clonal hematopoiesis is associated with attenuated response to inflammation and aging. *Cell Stem Cell*. 31:1127–1144.e17. https://doi.org/10.1016/j.stem.2024.05.010

Jang, G., S. Contreras Castillo, E. Esteva, S. Upadhaya, J. Feng, N.M. Adams, E. Richard, R. Awatramani, C.M. Sawai, and B. Reizis. 2023. Stem cell decoupling underlies impaired lymphoid development during aging. *Proc. Natl. Acad. Sci. USA*. 120:e2302019120. https://doi.org/10.1073/pnas.2302019120

Kanayama, M., S. Xu, K. Danzaki, J.R. Gibson, M. Inoue, S.G. Gregory, and M.L. Shinohara. 2017. Skewing of the population balance of lymphoid and myeloid cells by secreted and intracellular osteopontin. *Nat. Immunol*. 18:973–984. https://doi.org/10.1038/ni.3791

Kasbekar, M., C.A. Mitchell, M.A. Proven, and E. Passegué. 2023. Hematopoietic stem cells through the ages: A lifetime of adaptation to organismal demands. *Cell Stem Cell*. 30:1403–1420. https://doi.org/10.1016/j.stem.2023.09.013

Khodadadi-Jamayran, A., and A. Tsirigos. 2020. Graph drawing-based dimensionality reduction to identify hidden communities in single-cell sequencing spatial representation. *bioRxiv*. https://doi.org/10.1101/2020.05.05.078550 (Preprint posted May 5, 2020).

King, K.Y., Y. Huang, D. Nakada, and M.A. Goodell. 2020. Environmental influences on clonal hematopoiesis. *Exp. Hematol*. 83:66–73. https://doi.org/10.1016/j.exphem.2019.12.005

Kishtagari, A., R.L. Levine, and A.D. Viny. 2020. Driver mutations in acute myeloid leukemia. *Curr. Opin. Hematol*. 27:49–57. https://doi.org/10.1097/MOH.0000000000000567

Ko, M., H.S. Bandukwala, J. An, E.D. Lamperti, E.C. Thompson, R. Hastie, A. Tsangaratou, K. Rajewsky, S.B. Koralov, and A. Rao. 2011. Ten-Eleven-Translocation 2 (TET2) negatively regulates homeostasis and differentiation of hematopoietic stem cells in mice. *Proc. Natl. Acad. Sci. USA*. 108:14566–14571. https://doi.org/10.1073/pnas.1112317108

Kortum, R.L., A.K. Rouquette-Jazdanian, and L.E. Samelson. 2013. Ras and extracellular signal-regulated kinase signaling in thymocytes and T cells. *Trends Immunol*. 34:259–268. https://doi.org/10.1016/j.it.2013.02.004

Köthe, S., J.P. Müller, S.A. Böhmer, T. Tschongov, M. Fricke, S. Koch, C. Thiede, R.P. Requardt, I. Rubio, and F.D. Böhmer. 2013. Features of ras activation by a mislocalized oncogenic tyrosine kinase: FLT3 ITD signals through K-Ras at the plasma membrane of acute myeloid leukemia cells. *J. Cell Sci*. 126:4746–4755. https://doi.org/10.1242/jcs.131789

Laurenti, E., and B. Göttgens. 2018. From haematopoietic stem cells to complex differentiation landscapes. *Nature*. 553:418–426. https://doi.org/10.1038/nature25022

Li, L.X., C.A. Goetz, C.D. Katerndahl, N. Sakaguchi, and M.A. Farrar. 2010. A Flt3- and Ras-dependent pathway primes B cell development by inducing a state of IL-7 responsiveness. *J. Immunol*. 184:1728–1736. https://doi.org/10.4049/jimmunol.0903023

Li, Z., X. Cai, C.L. Cai, J. Wang, W. Zhang, B.E. Petersen, F.C. Yang, and M. Xu. 2011. Deletion of Tet2 in mice leads to dysregulated hematopoietic stem cells and subsequent development of myeloid malignancies. *Blood*. 118: 4509–4518. https://doi.org/10.1182/blood-2010-12-325241

Liaw, L., D.E. Birk, C.B. Ballas, J.S. Whitsitt, J.M. Davidson, and B.L. Hogan. 1998. Altered wound healing in mice lacking a functional osteopontin gene (spp1). *J. Clin. Invest*. 101:1468–1478. https://doi.org/10.1172/JCI2131

Liersch, R., J. Gerss, C. Schliemann, M. Bayer, C. Schwöppe, C. Biermann, I. Appelmann, T. Kessler, B. Löwenberg, T. Büchner, et al. 2012. Osteopontin is a prognostic factor for survival of acute myeloid leukemia patients. *Blood*. 119:5215–5220. https://doi.org/10.1182/blood-2011-11-389692

McMahon, C.M., T. Ferng, J. Canaani, E.S. Wang, J.J.D. Morrissette, D.J. Eastburn, M. Pellegrino, R. Durruthy-Durruthy, C.D. Watt, S. Asthana, et al. 2019. Clonal selection with RAS pathway activation mediates secondary clinical resistance to selective FLT3 inhibition in acute myeloid leukemia. *Cancer Discov*. 9:1050–1063. https://doi.org/10.1158/2159-8290.CD-18-1453

Meisel, M., R. Hinterleitner, A. Pacis, L. Chen, Z.M. Earley, T. Mayassi, J.F. Pierre, J.D. Ernest, H.J. Galipeau, N. Thuille, et al. 2018. Microbial signals drive pre-leukaemic myeloproliferation in a Tet2-deficient host. *Nature*. 557:580–584. https://doi.org/10.1038/s41586-018-0125-z

Miles, L.A., R.L. Bowman, T.R. Merlinsky, I.S. Csete, A.T. Ooi, R. Durruthy-Durruthy, M. Bowman, C. Famulare, M.A. Patel, P. Mendez, et al. 2020. Single-cell mutation analysis of clonal evolution in myeloid malignancies. *Nature*. 587:477–482. https://doi.org/10.1038/s41586-020-2864-x

Moran-Crusio, K., L. Reavie, A. Shih, O. Abdel-Wahab, D. Ndiaye-Lobry, C. Lobry, M.E. Figueroa, A. Vasanthakumar, J. Patel, X. Zhao, et al. 2011. Tet2 loss leads to increased hematopoietic stem cell self-renewal and myeloid transformation. *Cancer Cell*. 20:11–24. https://doi.org/10.1016/j.ccr.2011.06.001

Morita, K., F. Wang, K. Jahn, T. Hu, T. Tanaka, Y. Sasaki, J. Kuipers, S. Loghavi, S.A. Wang, Y. Yan, et al. 2020. Clonal evolution of acute myeloid leukemia revealed by high-throughput single-cell genomics. *Nat. Commun*. 11:5327. https://doi.org/10.1038/s41467-020-19119-8

Nam, A.S., N. Dusaj, F. Izzo, R. Murali, R.M. Myers, T.H. Mouhieddine, J. Sotelo, S. Benbarche, M. Waarts, F. Gaiti, et al. 2022. Single-cell multiomics of human clonal hematopoiesis reveals that DNMT3A R882 mutations perturb early progenitor states through selective hypomethylation. *Nat. Genet*. 54:1514–1526. https://doi.org/10.1038/s41588-022-01179-9

Okudela, K., H. Hayashi, T. Ito, T. Yazawa, T. Suzuki, Y. Nakane, H. Sato, H. Ishi, X. KeQin, A. Masuda, et al. 2004. K-Ras gene mutation enhances motility of immortalized airway cells and lung adenocarcinoma cells via akt activation: Possible contribution to non-invasive expansion of lung adenocarcinoma. *Am. J. Pathol*. 164:91–100. https://doi.org/10.1016/S0002-9440(10)63100-8

Passaro, D., M. Irigoyen, C. Catherinet, S. Gachet, C. Da Costa De Jesus, C. Lasgi, C. Tran Quang, and J. Ghysdael. 2015. CXCR4 is required for leukemia-initiating cell activity in T cell acute lymphoblastic leukemia. *Cancer Cell*. 27:769–779. https://doi.org/10.1016/j.ccell.2015.05.003

Peng, S.B., X. Zhang, D. Paul, L.M. Kays, W. Gough, J. Stewart, M.T. Uhlik, Q. Chen, Y.H. Hui, M.J. Zamek-Gliszczynski, et al. 2015. Identification of LY2510924, a novel cyclic peptide CXCR4 antagonist that exhibits antitumor activities in solid tumor and breast cancer metastatic models. *Mol. Cancer Ther*. 14:480–490. https://doi.org/10.1158/1535-7163.MCT-14-0850

Pietras, E.M., D. Reynaud, Y.A. Kang, D. Carlin, F.J. Calero-Nieto, A.D. Leavitt, J.M. Stuart, B. Göttgens, and E. Passegué. 2015. Functionally distinct subsets of lineage-biased multipotent progenitors control blood production in normal and regenerative conditions. *Cell Stem Cell*. 17:35–46. https://doi.org/10.1016/j.stem.2015.05.003

Pitt, L.A., A.N. Tikhonova, H. Hu, T. Trimarchi, B. King, Y. Gong, M. Sanchez-Martin, A. Tsirigos, D.R. Littman, A.A. Ferrando, et al. 2015. CXCL12-Producing vascular endothelial niches control acute T cell leukemia maintenance. *Cancer Cell*. 27:755–768. https://doi.org/10.1016/j.ccell.2015.05.002

Pollock, C.B., S. Shirasawa, T. Sasazuki, W. Kolch, and A.S. Dhillon. 2005. Oncogenic K-RAS is required to maintain changes in cytoskeletal organization, adhesion, and motility in colon cancer cells. *Cancer Res*. 65: 1244–1250. https://doi.org/10.1158/0008-5472.CAN-04-1911

Pollyea, D.A., and C.T. Jordan. 2017. Therapeutic targeting of acute myeloid leukemia stem cells. *Blood*. 129:1627–1635. https://doi.org/10.1182/blood-2016-10-696039

Pucella, J.N., S. Upadhaya, and B. Reizis. 2020. The source and dynamics of adult hematopoiesis: Insights from lineage tracing. *Annu. Rev. Cell Dev.*

Biol. 36:529–550. https://doi.org/10.1146/annurev-cellbio-020520-114601

Quivoron, C., L. Couronné, V. Della Valle, C.K. Lopez, I. Plo, O. Wagner-Ballon, M. Do Cruzeiro, F. Delhommeau, B. Arnulf, M.H. Stern, et al. 2011. TET2 inactivation results in pleiotropic hematopoietic abnormalities in mouse and is a recurrent event during human lymphomagenesis. *Cancer Cell.* 20:25–38. https://doi.org/10.1016/j.ccr.2011.06.003

Sabnis, A.J., L.S. Cheung, M. Dail, H.C. Kang, M. Santaguida, M.L. Hermiston, E. Passegué, K. Shannon, and B.S. Braun. 2009. Oncogenic Kras initiates leukemia in hematopoietic stem cells. *PLoS Biol.* 7:e59. https://doi.org/10.1371/journal.pbio.1000059

Sankaran, V.G., J.S. Weissman, and L.I. Zon. 2022. Cellular barcoding to decipher clonal dynamics in disease. *Science.* 378:eabm5874. https://doi.org/10.1126/science.abm5874

Sawai, C.M., S. Babovic, S. Upadhaya, D.J.H.F. Knapp, Y. Lavin, C.M. Lau, A. Goloborodko, J. Feng, J. Fujisaki, L. Ding, et al. 2016. Hematopoietic stem cells are the major source of multilineage hematopoiesis in adult animals. *Immunity.* 45:597–609. https://doi.org/10.1016/j.immuni.2016.08.007

Säwen, P., M. Eldeeb, E. Erlandsson, T.A. Kristiansen, C. Laterza, Z. Kokaia, G. Karlsson, J. Yuan, S. Soneji, P.K. Mandal, et al. 2018. Murine HSCs contribute actively to native hematopoiesis but with reduced differentiation capacity upon aging. *Elife.* 7:e41258. https://doi.org/10.7554/eLife.41258

Schepers, K., T.B. Campbell, and E. Passegué. 2015. Normal and leukemic stem cell niches: Insights and therapeutic opportunities. *Cell Stem Cell.* 16:254–267. https://doi.org/10.1016/j.stem.2015.02.014

Schiroli, G., V. Kartha, F.M. Duarte, T.A. Kristiansen, C. Mayerhofer, R. Shrestha, A. Earl, Y. Hu, T. Tay, C. Rhee, et al. 2024. Cell of origin epigenetic priming determines susceptibility to Tet2 mutation. *Nat. Commun.* 15:4325. https://doi.org/10.1038/s41467-024-48508-6

Schwede, M., K. Jahn, J. Kuipers, L.A. Miles, R.L. Bowman, T. Robinson, K. Furudate, H. Uryu, T. Tanaka, Y. Sasaki, et al. 2023. Mutation order in acute myeloid leukemia identifies uncommon patterns of evolution and illuminates phenotypic heterogeneity. *Res. Sq.* https://doi.org/10.21203/rs.3.rs-3516536/v1 (Preprint posted November 6, 2023).

Snoeck, H.W. 2017. Mitochondrial regulation of hematopoietic stem cells. *Curr. Opin. Cell Biol.* 49:91–98. https://doi.org/10.1016/j.ceb.2017.12.010

Stier, S., Y. Ko, R. Forkert, C. Lutz, T. Neuhaus, E. Grünewald, T. Cheng, D. Dombkowski, L.M. Calvi, S.R. Rittling, and D.T. Scadden. 2005. Osteopontin is a hematopoietic stem cell niche component that negatively regulates stem cell pool size. *J. Exp. Med.* 201:1781–1791. https://doi.org/10.1084/jem.20041992

Stoeckius, M., S. Zheng, B. Houck-Loomis, S. Hao, B.Z. Yeung, W.M. Mauck III, P. Smibert, and R. Satija. 2018. Cell Hashing with barcoded antibodies enables multiplexing and doublet detection for single cell genomics. *Genome Biol.* 19:224. https://doi.org/10.1186/s13059-018-1603-1

Tarnawsky, S.P., M. Kobayashi, R.J. Chan, and M.C. Yoder. 2017. Mice expressing KrasG12D in hematopoietic multipotent progenitor cells develop neonatal myeloid leukemia. *J. Clin. Invest.* 127:3652–3656. https://doi.org/10.1172/JCI94031

Tuveson, D.A., A.T. Shaw, N.A. Willis, D.P. Silver, E.L. Jackson, S. Chang, K.L. Mercer, R. Grochow, H. Hock, D. Crowley, et al. 2004. Endogenous oncogenic K-ras(G12D) stimulates proliferation and widespread neoplastic and developmental defects. *Cancer Cell.* 5:375–387. https://doi.org/10.1016/S1535-6108(04)00085-6

Upadhaya, S., O. Krichevsky, I. Akhmetzyanova, C.M. Sawai, D.R. Fooksman, and B. Reizis. 2020. Intravital imaging reveals motility of adult hematopoietic stem cells in the bone marrow niche. *Cell Stem Cell.* 27:336–345.e4. https://doi.org/10.1016/j.stem.2020.06.003

Upadhaya, S., C.M. Sawai, E. Papalexi, A. Rashidfarrokhi, G. Jang, P. Chattopadhyay, R. Satija, and B. Reizis. 2018. Kinetics of adult hematopoietic stem cell differentiation in vivo. *J. Exp. Med.* 215:2815–2832. https://doi.org/10.1084/jem.20180136

Van Egeren, D., J. Escabi, M. Nguyen, S. Liu, C.R. Reilly, S. Patel, B. Kamaz, M. Kalyva, D.J. DeAngelo, I. Galinsky, et al. 2021. Reconstructing the lineage histories and differentiation trajectories of individual cancer cells in myeloproliferative neoplasms. *Cell Stem Cell.* 28:514–523.e9. https://doi.org/10.1016/j.stem.2021.02.001

Van Meter, M.E., E. Díaz-Flores, J.A. Archard, E. Passegué, J.M. Irish, N. Kotecha, G.P. Nolan, K. Shannon, and B.S. Braun. 2007. K-RasG12D expression induces hyperproliferation and aberrant signaling in primary hematopoietic stem/progenitor cells. *Blood.* 109:3945–3952. https://doi.org/10.1182/blood-2006-09-047530

Wang, M., J. Han, L. Marcar, J. Black, Q. Liu, X. Li, K. Nagulapalli, L.V. Sequist, R.H. Mak, C.H. Benes, et al. 2017. Radiation resistance in KRAS-mutated lung cancer is enabled by stem-like properties mediated by an osteopontin-EGFR pathway. *Cancer Res.* 77:2018–2028. https://doi.org/10.1158/0008-5472.CAN-16-0808

Wang, X., S. Allen, J.F. Blake, V. Bowcut, D.M. Briere, A. Calinisan, J.R. Dahlke, J.B. Fell, J.P. Fischer, R.J. Gunn, et al. 2022. Identification of MRTX1133, a noncovalent, potent, and selective $KRAS^{G12D}$ inhibitor. *J. Med. Chem.* 65:3123–3133. https://doi.org/10.1021/acs.jmedchem.1c01688

Warren, J.T., and D.C. Link. 2020. Clonal hematopoiesis and risk for hematologic malignancy. *Blood.* 136:1599–1605. https://doi.org/10.1182/blood.2019000991

Weeks, L.D., and B.L. Ebert. 2023. Causes and consequences of clonal hematopoiesis. *Blood.* 142:2235–2246. https://doi.org/10.1182/blood.2023022222

Wei, D., L. Wang, X. Zuo, A. Maitra, and R.S. Bresalier. 2024. A small molecule with big impact: MRTX1133 targets the KRASG12D mutation in pancreatic cancer. *Clin. Cancer Res.* 30:655–662. https://doi.org/10.1158/1078-0432.CCR-23-2098

Yamashita, M., P.V. Dellorusso, O.C. Olson, and E. Passegué. 2020. Dysregulated haematopoietic stem cell behaviour in myeloid leukaemogenesis. *Nat. Rev. Cancer.* 20:365–382. https://doi.org/10.1038/s41568-020-0260-3

Yamashita, M., and E. Passegué. 2019. TNF-α coordinates hematopoietic stem cell survival and myeloid regeneration. *Cell Stem Cell.* 25:357–372.e7. https://doi.org/10.1016/j.stem.2019.05.019

Zehentmeier, S., V.Y. Lim, Y. Ma, J. Fossati, T. Ito, Y. Jiang, A.V. Tumanov, H.J. Lee, L. Dillinger, J. Kim, et al. 2022. Dysregulated stem cell niches and altered lymphocyte recirculation cause B and T cell lymphopenia in WHIM syndrome. *Sci. Immunol.* 7:eabo3170. https://doi.org/10.1126/sciimmunol.abo3170

Zhou, J., X. Chen, P. Zhou, X. Sun, Y. Chen, M. Li, Y. Chu, J. Zhou, X. Hu, Y. Luo, et al. 2022. Osteopontin is required for the maintenance of leukemia stem cells in acute myeloid leukemia. *Biochem. Biophys. Res. Commun.* 600:29–34. https://doi.org/10.1016/j.bbrc.2022.02.022

JEM

Supplemental material

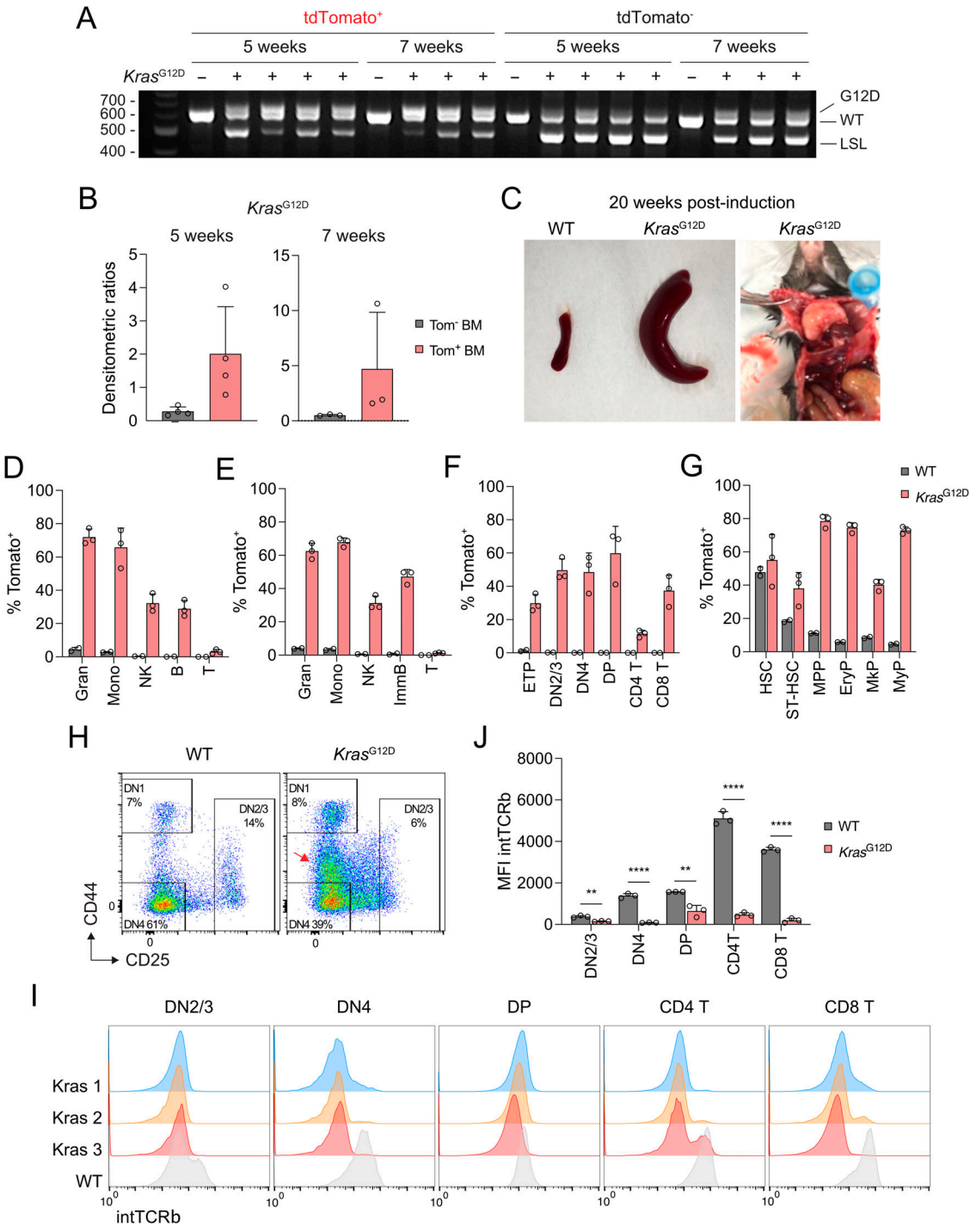

Figure S1. ***Kras*^{G12D} mutation in HSC causes aberrant thymocyte development and T-cell lymphoma. (A)** *Kras*^{G12D} activation in Tom$^+$ or Tom$^-$ BM cells after Cre recombination. PCR was performed on DNA extracted from Tom$^+$ or Tom$^-$ total BM cells at 5 or 7 wk after tamoxifen induction. PCR products corresponding to the WT (622-bp), unrecombined LSL (500-bp), and the Cre-recombined *Kras*^{G12D} (G12D, 650-bp) alleles are indicated. Each lane represents an individual mouse. **(B)** Densitometric ratios of the recombined (G12D)-to-unrecombined (LSL) amplicons for the genotyping data in panel A. Symbols represent individual mice; bars represent the mean ± SD. **(C)** Representative gross morphology of *Pdzk1ip1*-CreER *R26*$^{Tom/Tom}$ *Kras*^{G12D} reporter mice showing splenomegaly and enlarged thymus after 20 wk after tamoxifen treatment. **(D–G)** Analysis of *Pdzk1ip1*-CreER *R26*$^{Tom/Tom}$ WT or *Kras*^{G12D} reporter mice at 7 wk after tamoxifen administration. Symbols represent individual mice; bars represent the mean ± SD. Shown are fractions of Tom$^+$ cells in mature cells in the spleen (D) and in the BM (E), thymocyte subsets (F), and stem/progenitors in the BM (G). **(H)** Representative flow cytometry plots of gated double-negative (CD4$^-$ CD8$^-$) thymocyte population in *Pdzk1ip1*-CreER *R26*$^{Tom/Tom}$ WT or *Kras*^{G12D} mice. DN1–DN4 subsets are highlighted; red arrows indicate the expanded intermediate subsets. **(I)** Representative histogram of intracellular TCRβ expression in the indicated thymocyte subsets. DN2/3, CD4$^-$ CD8$^-$ CD25$^+$; DN4, CD4$^-$ CD8$^-$ CD25$^-$ CD44$^-$; DP, CD4$^+$ CD8$^+$; CD4 T, CD4$^+$ CD8$^-$; CD8 T, CD4$^-$ CD8$^+$. **(J)** MFI of intracellular TCRβ expression in the indicated thymocyte subsets. Symbols represent individual mice; bars represent the mean ± SD. Given the expected normal distribution of fluorescence intensities, statistical significance was evaluated using Student's *t* test. **P < 0.01, ****P < 0.0001. MFI, mean fluorescence intensity. Source data are available for this figure: SourceData FS1.

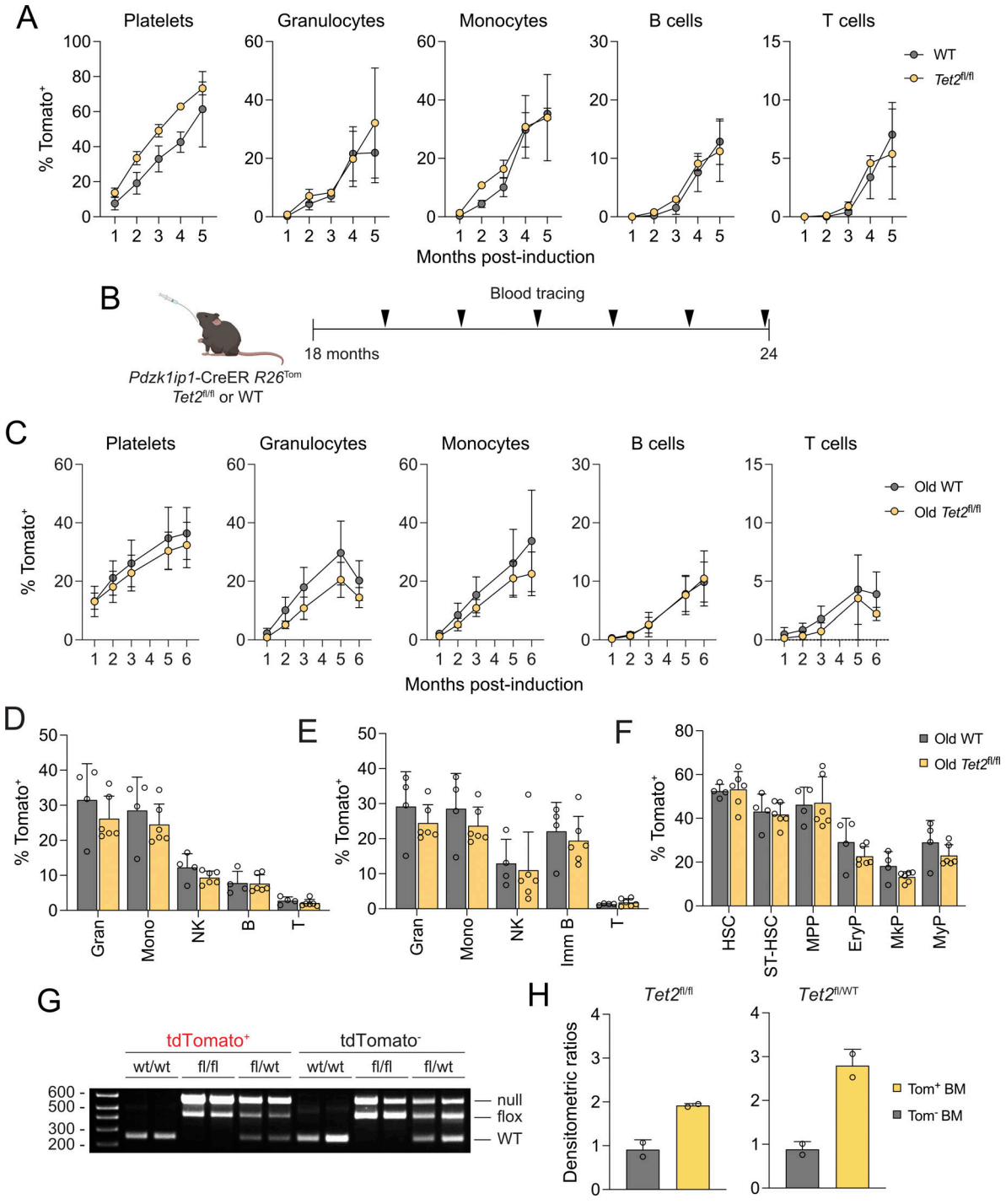

Figure S2. ***Tet2*-deficient HSC do not show increased contribution to hematopoiesis. (A)** *Pdzk1ip1*-CreER *R26*$^{Tom/Tom}$ mice were crossed with the Cre-inducible null *Tet2* (*Tet2*$^{fl/fl}$) allele. *Tet2*$^{fl/fl}$ or WT reporter mice were induced with tamoxifen (0.5 mg), and Tom expression in the PB was analyzed monthly. Shown are the fractions of Tom$^+$ cells in the indicated cell types. Symbols represent the mean ± SD of *Tet2*$^{fl/fl}$ (n = 2) or WT (n = 2) reporter animals. **(B)** *Tet2*$^{fl/fl}$ or WT reporter animals were aged for 18 mo and treated with tamoxifen (1 mg), and the accrual of labeled Tom$^+$ cells was examined monthly (arrowheads) in PB. After 6 mo, *Tet2*$^{fl/fl}$ or WT mice were sacrificed for the endpoint analysis. **(C)** Cell labeling in the PB. Shown are fractions of Tom$^+$ cells in the indicated blood cell types in old *Tet2*$^{fl/fl}$ or WT mice at the indicated time points after tamoxifen treatment. Symbols represent the mean ± SD of *Tet2*$^{fl/fl}$ (n = 6) or WT (n = 4) reporter animals. **(D–F)** Accrual of Tom$^+$ cells at the endpoint. Shown are fractions of Tom$^+$ cells in the mature cell types in the spleen (D) and BM (E), and in stem/progenitor cell populations (F). Symbols represent individual mice; bars represent the mean ± SD; data are from a single experiment. No statistically significant differences were observed. **(G)** Cre-induced *Tet2*^{fl} recombination in Tom$^+$ or Tom$^-$ total BM cells 6 mo after tamoxifen treatment. Genomic PCR was performed on DNA extracted from Tom$^+$ or Tom$^-$ cells sorted from WT, *Tet2*$^{fl/fl}$, or *Tet2*$^{fl/wt}$ reporter mice; each lane represents an individual mouse. PCR products corresponding to the WT (250-bp), unrecombined *Tet2*^{fl} (flox, 430-bp), and Cre-recombined *Tet2*^{fl} (null, 550-bp) alleles are indicated. **(H)** Densitometric ratios of the recombined (null)-to-unrecombined (flox) amplicons for the genotyping data in panel G. Symbols represent individual mice; bars represent the mean ± range. Source data are available for this figure: SourceData FS2.

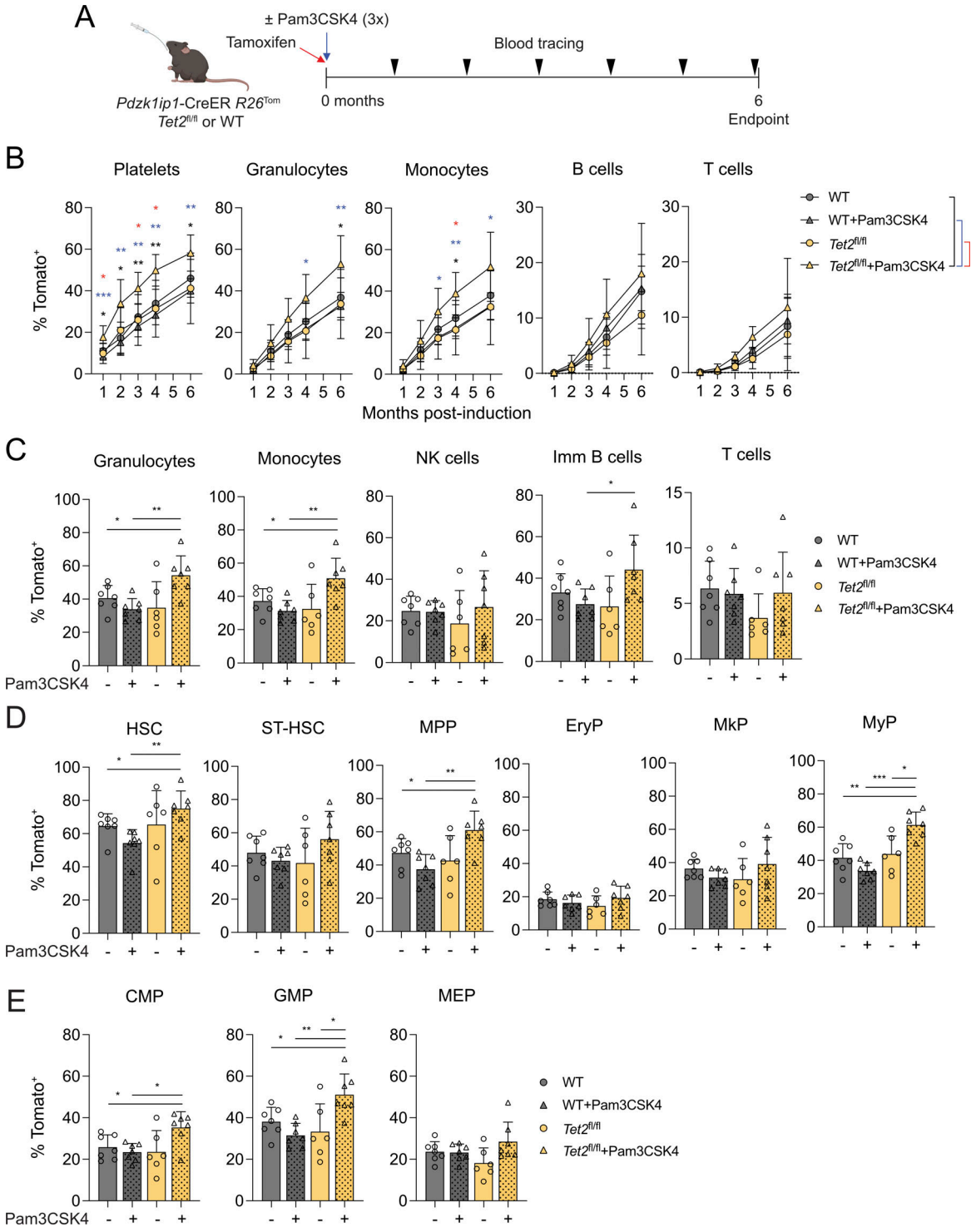

Figure S3. ***Tet2*-deficient HSC show increased contribution to myelopoiesis after inflammatory stimulation. (A)** Lineage tracing of *Tet2*-deficient HSC after stimulation with the TLR2 agonist Pam3CSK4. HSC-specific Cre reporter mice (*Pdzk1ip1*-CreER *R26*$^{Tom/Tom}$) that carried WT or conditional null (*Tet2*$^{fl/fl}$) *Tet2* alleles were administered a single dose of tamoxifen to induce simultaneous Tom expression and *Tet2* deletion in HSC, with or without simultaneous treatment with the TLR2 agonist Pam3CSK4 for three consecutive days. Mice were monitored monthly for Tom expression in PB (arrowheads) and analyzed at the 6-mo endpoint. **(B)** Accrual of Tom$^+$ cells in the blood over time. Shown are fractions of Tom$^+$ cells within the indicated blood cell type in *Tet2*$^{fl/fl}$ or WT reporter mice with or without Pam3CSK4 treatment at the indicated monthly intervals after the induction. Symbols represent the mean ± SD of six to eight mice per group pooled from two experiments. Asterisks indicate significant differences between WT versus *Tet2*$^{fl/fl}$+Pam3CSK4 (black), WT+Pam3CSK4 versus *Tet2*$^{fl/fl}$+Pam3CSK4 (blue), or *Tet2*$^{fl/fl}$ versus *Tet2*$^{fl/fl}$+Pam3CSK4 (red). **(C–E)** Accrual of Tom$^+$ cells in the BM at the endpoint. Shown are fractions of Tom$^+$ cells in the mature cell types in the BM (C), in stem/progenitor cell populations (D), and in lineage-committed MyP (E). CMP, common myeloid progenitor; GMP, granulocyte/monocyte progenitor. Symbols represent individual mice; bars represent the mean ± SD; data are pooled from two independent experiments. Statistical significance was estimated by the Mann–Whitney test. *P < 0.05, **P < 0.01, ***P < 0.001.

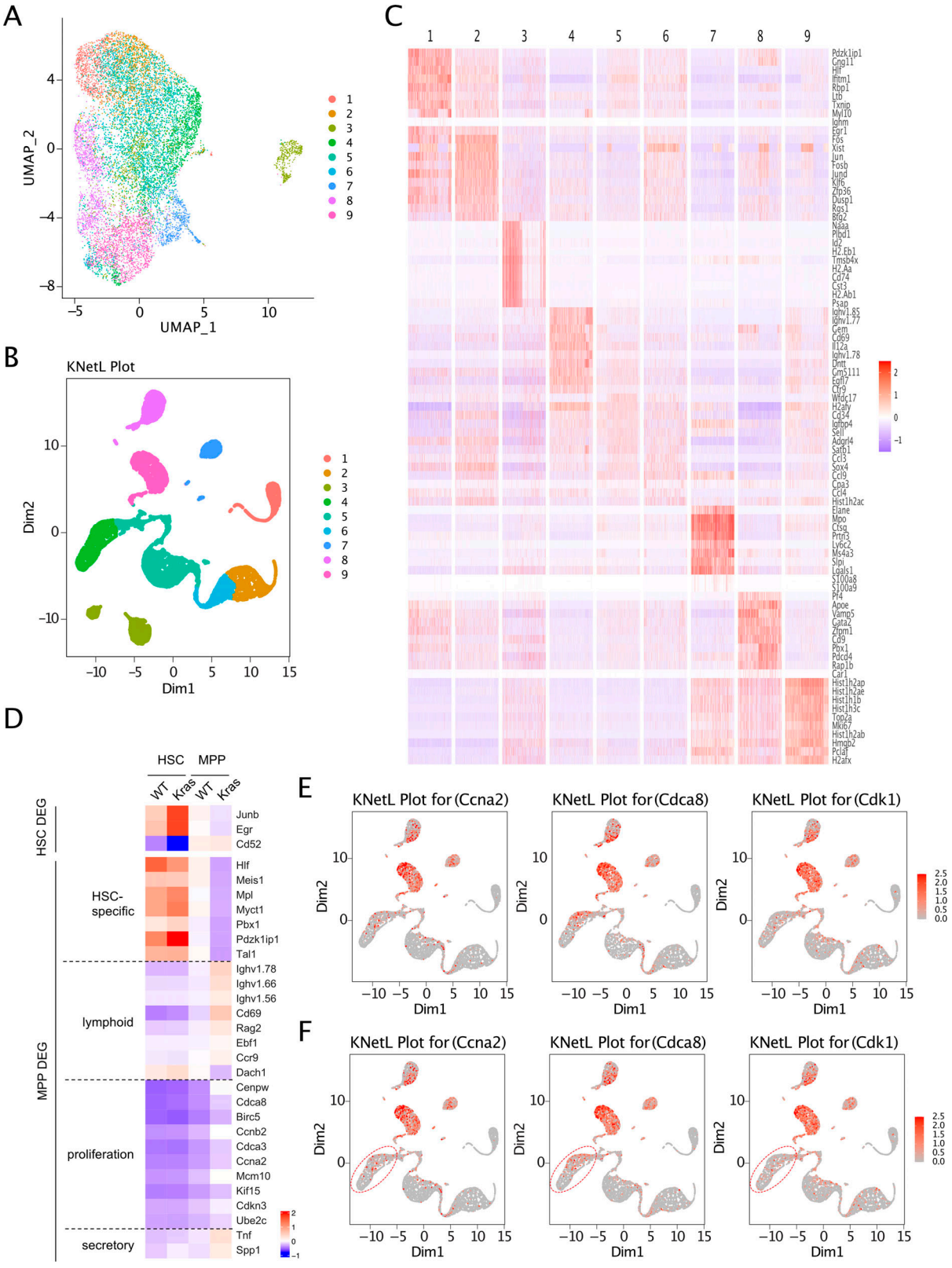

Figure S4. **Additional CITE-seq analysis. (A)** UMAP plot of single cells clustered by transcriptomic data. Cells are colored according to clusters generated by the KNetL algorithm. **(B)** KNetL plot of single cells colored by cluster. **(C)** Heatmap of top 10 marker genes (rows) in individual cells (columns) for each cluster. **(D)** Heatmap showing select DEG between *Kras*^{G12D} and WT cells within the HSC or MPP clusters. Average expression of DEG representing HSC-specific, lymphoid, proliferation-associated, or secreted products is shown according to the indicated color scale. **(E and F)** Feature plots showing the expression of lymphoid development–associated genes (E) and proliferation-associated genes (F) in individual cells on the KNetL plot. The *Kras*^{G12D}-specific MPP cluster is highlighted. UMAP, Uniform Manifold Approximation and Projection.

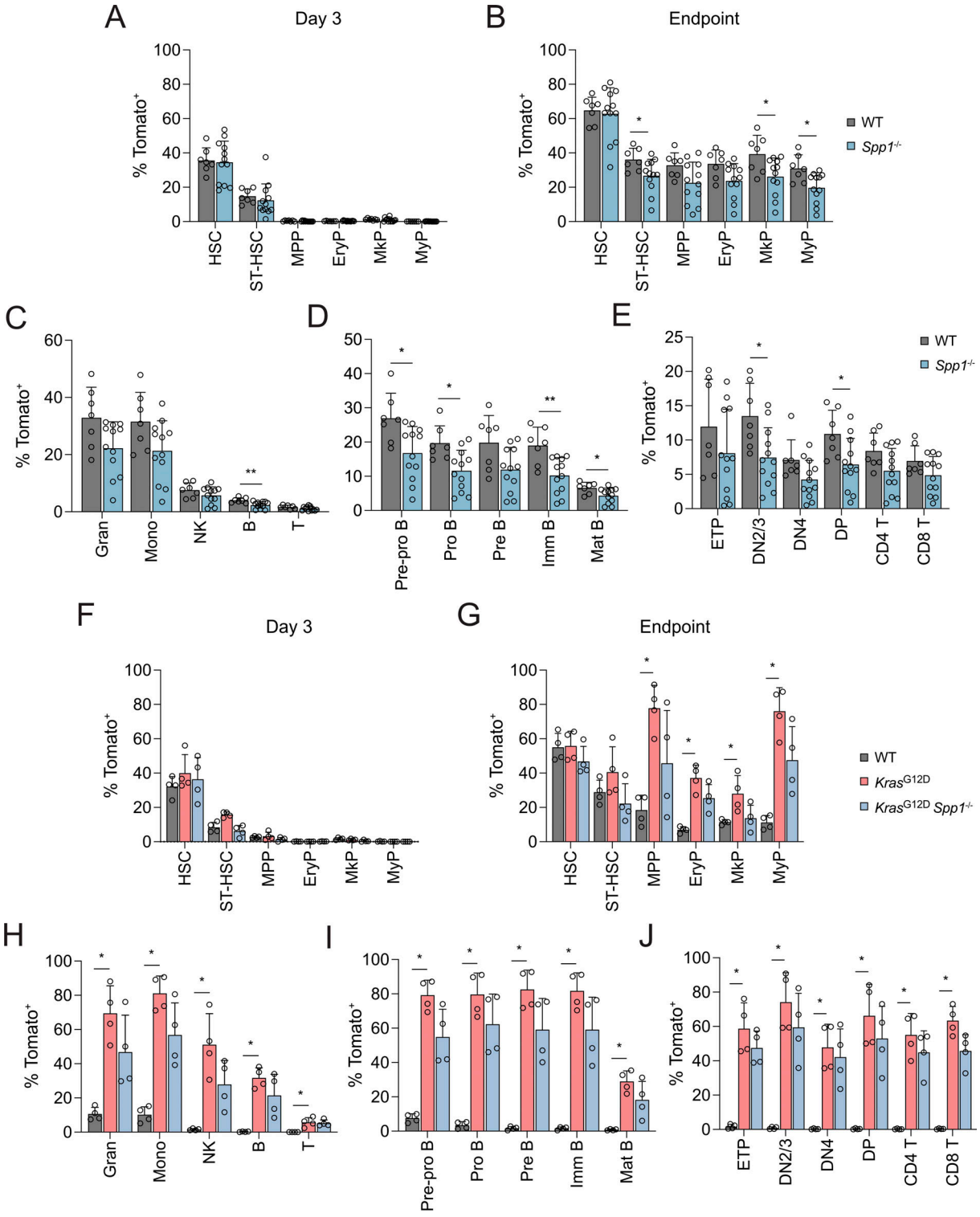

Figure S5. **Additional characterization of HSC contribution in osteopontin-deficient mice. (A–E)** Analysis of *Pdzk1ip1*-CreER *R26*$^{Tom/Tom}$ WT (*Spp1*$^{+/+}$) or *Spp1*$^{-/-}$ reporter mice at 12 wk after tamoxifen administration. Symbols represent individual mice, and bars represent the mean ± SD; data were pooled from two experiments. **(A)** Fractions of Tom$^+$ cells in BM stem/progenitor cells at day 3 post-after tamoxifen treatment as determined by BM biopsy. **(B)** Fractions of Tom$^+$ cells in BM stem/progenitor cells at the 12-wk endpoint. **(C–E)** Fractions of Tom$^+$ cells in mature cell types in the spleen (C), subsets of B cells in the BM (D), and thymocyte subsets (E) at the endpoint. **(F–J)** Analysis of *Pdzk1ip1*-CreER *R26*$^{Tom/Tom}$ WT, *Kras*^{G12D}, or *Kras*^{G12D} *Spp1*$^{-/-}$ reporter mice at 7 wk after tamoxifen administration. **(F)** Fractions of Tom$^+$ cells in BM stem/progenitor cells at day 3 after tamoxifen treatment as determined by BM biopsy. Symbols represent individual mice, and bars represent the mean ± SD; data are from a single experiment. **(G)** Fractions of Tom$^+$ cells in BM stem/progenitor cells at the 7-wk endpoint. **(H–J)** Fractions of Tom$^+$ cells in mature cell types in the spleen (H), subsets of B cells in the BM (I), and thymocyte subsets (J) at the endpoint. In all panels, symbols represent individual mice and bars represent the mean ± SD. Statistical significance was estimated by the Mann–Whitney test. *P < 0.05, **P < 0.01.

Video 1. **Representative video microscopy of Tom⁺ stem/progenitor cells in the tibia of live WT or *Kras*^{G12D} reporter mice at 2 wk after tamoxifen induction.** Images on the left and right sides show recordings from WT or *Kras*^{G12D} reporter mice, respectively, with the tracks of select Tom⁺ cells indicated by multiple colors. The scale bar is indicated on the lower left. The scale in the upper center indicates time in hours:minutes:seconds:milliseconds. Playback speed 507×.

Video 2. **Representative video microscopy of Tom⁺ stem/progenitor cells in the tibia of live WT or *Kras*^{G12D} reporter mice at 3 wk after tamoxifen induction.** Images on the left and right sides show recordings from WT or *Kras*^{G12D} reporter mice, respectively, with the tracks of select Tom⁺ cells indicated by multiple colors. The scale bar is indicated on the lower left. The scale in the upper center indicates time in hours:minutes:seconds:milliseconds. Playback speed 467×.

Video 3. **Representative video microscopy of Tom⁺ stem/progenitor cells in the tibia of live LY2510924-treated WT reporter mice at 3 wk after tamoxifen induction.** The image shows recordings before and after LY2510924 administration, with the tracks of select Tom⁺ cells indicated by multiple colors. The scale bar is indicated on the lower left. The scale in the lower right indicates time in hours:minutes:seconds:milliseconds. Playback speed 470×.

Video 4. **Representative video microscopy of Tom⁺ stem/progenitor cells in the tibia of live LY2510924-treated *Kras*^{G12D} reporter mice at 3 wk after tamoxifen induction.** The image shows recordings before and after LY2510924 administration, with the tracks of select Tom⁺ cells indicated by multiple colors. The scale bar is indicated on the lower left. The scale in the lower right indicates time in hours:minutes:seconds:milliseconds. Playback speed 470×.

Provided online are Table S1, Table S2, and Table S3. Table S1 shows DEG in CITE-seq cell clusters. Table S2 shows DEG between WT and Kras-mutant cells. Table S3 shows antibodies and reagents.